Draft version July 20, 2021
Typeset using LATEX twocolumn style in AASTeX63

# Gravitational wave sources in our Galactic backyard: Predictions for BH and NS binaries in LISA

T. Wagg,[1,2] F. Broekgaarden,[1] S. E. de Mink,[2,3,1] N. Frankel,[4] L.A.C. van Son,[1,3,2] and S. Justham[5,3,2]

[1] Center for Astrophysics — Harvard & Smithsonian, 60 Garden Street, Cambridge, MA 02138, USA
[2] Max-Planck-Institut für Astrophysik, Karl-Schwarzschild-Straße 1, 85741 Garching, Germany
[3] Anton Pannekoek Institute for Astronomy & Grappa, University of Amsterdam, Postbus 94249, 1090 GE Amsterdam, The Netherlands
[4] Max Planck Institute for Astronomy, Königstuhl 17, D-69117 Heidelberg, Germany
[5] School of Astronomy & Space Science, University of the Chinese Academy of Sciences, Beijing 100012, China

(Received July 20, 2021)

## ABSTRACT

We present predictions for the properties of the population of Galactic double black holes (BHBH), black hole neutron stars (BHNS) and double neutron stars (NSNS) that will be detectable by the planned space-based gravitational wave detector LISA. We use rapid population synthesis to produce an extensive sample of double compact objects (DCOs) and combine this with an empirically-informed model to distribute them in a Milky Way-like galaxy based on their birth metallicity. We investigate the dependence of our results upon underlying physics assumptions by comparing the results of 20 physics variations that vary assumptions relating to mass transfer, common envelope, supernova and wind mass loss physics. We find that for a 4(10)-year mission, LISA will detect on average about 36(56) BHBHs, 33(55) BHNSs, 8(13) NSNSs. The BHBH rate remains notably consistent under different physics assumptions, whilst in contrast the BHNS and NSNS rates each vary over 3 orders of magnitude. We discuss observable characteristics that could be used to distinguish the aforementioned DCOs from the more numerous double white dwarf population as well as for disentangling the BHBH, BHNS and NSNS populations from each other. We additionally assess the possibility of multi-messenger observations of pulsar populations by combining the capabilities of LISA and SKA.

*Keywords:* LISA, black hole, neutron star, binary

## 1. INTRODUCTION

Since the first direct observation of gravitational waves (Abbott et al. 2016), the number of black hole (BH) and neutron star (NS) binaries observed by ground-based gravitational-wave detectors has rapidly grown (Abbott et al. 2019, 2020b), offering exciting insights into the formation, lives and deaths of massive binary stars (e.g. Abbott et al. 2021).

The Laser Interferometer Space Antenna (LISA, Amaro-Seoane et al. 2017) will provide observations in an entirely new regime of gravitational waves. LISA will observe at lower frequencies than ground-based detectors ($10^{-5} \lesssim f/\,\mathrm{Hz} \lesssim 10^{-1}$) and so will enable the study of sources that are undetectable with ground-based detectors such as the mergers of supermassive black holes and extreme mass ratio inspirals (e.g. Begelman et al. 1980; Klein et al. 2016). Moreover, this frequency regime is also of interest for the detection of local stellar mass double compact objects (DCO) far in advance of their merger. This presents an opportunity for both multi-messenger detections to search for electromagnetic counterparts and multiband detections that can help to constrain binary characteristics (e.g. Sesana 2016; Gerosa et al. 2019). In addition, LISA will be able to measure the eccentricities of DCOs that may yield further constraints on binary evolution, differentiate between formation channels and distinguish between DCO types (e.g. Nelemans et al. 2001; Breivik et al. 2016; Antonini et al. 2017; Rodriguez et al. 2018). Unlike ground-based detectors, LISA only detects stellar mass sources in local galaxies, with the majority residing in the Milky Way. Therefore, these sources could be used as a probe for the structure of our galaxy (e.g. Korol et al. 2019).

Corresponding author: Tom Wagg
tomjwagg@gmail.com

Traditionally, investigations into detecting stellar mass sources with LISA focus on double white dwarf (WDWD) binaries, as they are abundantly present in our galaxy and are expected to be the dominant source of stellar-mass binaries that are detectable by LISA (Nelemans et al. 2001; Ruiter et al. 2010; Yu & Jeffery 2010; Nissanke et al. 2012; Korol et al. 2017; Lamberts et al. 2018). More recently, interest has grown in the detection of NS and BH binaries. Although they are more rare, LISA detections of these sources are potentially valuable for learning more about the evolution and endpoints of massive stars. In this paper we focus on double black hole binaries (BHBH), black hole neutron star binaries (BHNS) and double neutron star binaries (NSNS).

Galactic NSNSs have been observed with electromagnetic signals for several decades (e.g. Hulse & Taylor 1975; Tauris et al. 2017; Vigna-Gómez et al. 2018) and more recently the mergers of NSNS binaries with ground-based gravitational wave detectors have been detected (e.g. Abbott et al. 2017). The detection of a NSNS in LISA with a pulsar component could potentially connect these two populations if the binary is close to merging, as the binary could be observed from inspiral to merger. NSNS binaries are useful sources for understanding the origin of r-process elements (e.g. Eichler et al. 1989) as well as the electromagnetic counterparts to gravitational wave signal such as kilonovae (e.g. Metzger 2017), short gamma-ray bursts (e.g. Gompertz et al. 2020), radio emission (e.g. Hotokezaka et al. 2016) and neutrinos (e.g. Kyutoku et al. 2018).

BHBHs in the Milky Way present a greater observational challenge. To date, no BH has been observed to be in a binary with another compact object in the Milky Way and so LISA could provide the first detection of a Galactic BHBH. The only confirmed BHs in our galaxy have been discovered as components of X-ray binaries with companion stars (e.g. Bolton 1972; Webster & Murdin 1972). This sample of BHs has masses mainly constrained between 5 and 10 $\mathrm{M}_\odot$ (Corral-Santana et al. 2016), a stark contrast to the more massive BHs observed with LIGO/Virgo that tend to have masses concentrated around 30 $\mathrm{M}_\odot$ (Abbott et al. 2020b). These observations of X-ray binaries suggest the presence of a lower mass gap (from 2-5 $\mathrm{M}_\odot$) in which there are no strong candidates for either black holes or neutron stars (Özel et al. 2010; Farr et al. 2011) but the gap's existence remains an open question (e.g. Kreidberg et al. 2012; Mandel & Müller 2020). Recently there has also been increased discussion over the maximum BH mass in our galaxy, with the claims of a 70 $\mathrm{M}_\odot$ BH (Liu et al. 2019) which has subsequently been challenged (El-Badry & Quataert 2020; Abdul-Masih et al. 2020; Shenar et al. 2020; Eldridge et al. 2020) and revised measurements of the mass of Cygnus X-1 (Miller-Jones et al. 2021). A sample of BHBHs detected with LISA could possibly help to constrain the stellar mass BH mass distribution.

One particularly interesting class of potential LISA sources are BHNSs. With the recent detection of two BHNSs by the LIGO scientific collaboration, the existence of these DCOs has been confirmed (The LIGO Scientific Collaboration et al. 2021). However, with only two detections (not including the low-confidence candidates GW190425 and GW190184 (Abbott et al. 2020a,c)) and no electromagnetic counterparts, the formation rate and properties of BHNSs are still uncertain. Current predictions for the merger rate of BHNSs range across three orders of magnitude (e.g. Abadie et al. 2010; Broekgaarden et al. 2021) so the number of detections in LISA will be important in reducing this uncertainty, thereby refining our understanding of the remnants and evolution of massive stars. These binaries are expected to have electromagnetic counterparts that can studied in the same way as NSNSs. A distinctly exciting possibility is the detection of a pulsar–BH system or millisecond pulsar–BH system (Narayan et al. 1991). These systems could be observed not only by LISA, but also radio telescopes such as MeerKAT and SKA, which will help to improve the measurement of individual system parameters and to constrain uncertain binary evolution processes (e.g. Pfahl et al. 2005; Chattopadhyay et al. 2020).

For the purposes of this investigation, we consider the 'classical' isolated binary evolution channel (e.g. Tutukov & Yungelson 1973, 1993; Smarr & Blandford 1976; Srinivasan 1989; Kalogera et al. 2007; Belczynski et al. 2016) in which compact objects are formed through through common envelope ejection or a phase of highly non-conservative mass transfer (Heuvel 2011; van den Heuvel et al. 2017). We do not, however, account for several alternative proposed formation channels, which could affect the rate and distribution of detectable NS and BH binaries in LISA. These channels include: dynamical formation in dense star clusters (e.g. Sigurdsson & Hernquist 1993; Portegies Zwart & McMillan 2000; Miller & Lauburg 2009; Rodriguez et al. 2015) and (active) galactic nuclei discs (e.g. Morris 1993; Antonini & Rasio 2016; McKernan et al. 2020), isolated hierarchical triple evolution involving Kozai-Lidov oscillations (e.g. Stephan et al. 2016; Silsbee & Tremaine 2017; Antonini et al. 2017; Toonen et al. 2020) and chemically homogenous evolution through efficient rotational mixing (e.g. de Mink et al. 2009; de Mink & Mandel 2016; Marchant et al. 2016; du Buisson et al. 2020).

In this paper, we present predictions of the detection rate and distribution of binary properties (masses, frequency, eccentricity, distance, merger time) of BHBH, BHNS and NSNS binaries formed through isolated binary evolution in the Milky Way. We explore the effect of varying physical assumptions in our population synthesis model on our results as well as discuss the effect of extending the LISA mission length and the possibility of distinguishing detections.

Earlier work on BHBHs, BHNSs and NSNSs in LISA has used a variety of population synthesis codes, Milky Way models and LISA specifications, resulting in a wide range of predictions (Nelemans et al. 2001; Liu 2009; Belczynski et al. 2010; Liu & Zhang 2014; Lamberts et al. 2019; Lau et al. 2020; Breivik et al. 2020; Sesana et al. 2020). We build upon previous efforts but with several important improvements. We explore the effect of varying binary physics assumptions by repeating our analysis for 20 different models and comparing the effect on the detection rate and distributions of source parameters. We use a model for the Milky Way that accounts for the chemical enrichment history and calibrated on the latest APOGEE survey (Majewski et al. 2017; Frankel et al. 2018), whereas most others did not consider the effect of metallicity in detail (see however Lamberts et al. 2019; Sesana et al. 2020). We provide a full treatment of the eccentricity of detectable sources both for the inspiral evolution as well as gravitational wave signal during the LISA mission. Moreover, our binary population synthesis simulation is the most extensive of its kind to date and make use of the adaptive sampling algorithm STROOPWAFEL (Broekgaarden et al. 2019, 2021). Overall we simulate over 2 billion massive binaries to produce the DCO populations used in this work. We find that this large number of simulations is important to reduce the sampling noise.

All data produced in this study is publicly available on Zenodo [1] as is the population used in our simulations [2]. We make all code used to produce our results available in a Github repository [3]. In addition, the repository contains step-by-step Jupyter notebooks that explain how to reproduce and change each figure in the paper. In a companion paper, Wagg et al. (in prep), we present `LEGWORK`[4], a python package designed for making predictions for the detection of sources with LISA, which we use in this work.

[1] https://zenodo.org/record/4699713

[2] https://zenodo.org/record/4574727

[3] https://github.com/TomWagg/detecting-DCOs-in-LISA

[4] https://legwork.readthedocs.io

Our paper is structured as follows. In Section 2, we describe our methods for synthesising a population of binaries, the variations of physical assumptions that we consider, how we simulate the Milky Way distribution of DCOs and our methods for calculating a detection rate for LISA. We present our main results in Section 3, analysing our findings for each DCO type and variation of physical assumptions. In Section 5 we discuss these results. In Section 6, we compare and contrast our methods and findings to previous work and finish with our conclusions in Section 7.

## 2. METHOD

To produce predictions for the DCOs that are detectable with LISA, we synthesise a population of DCOs using the population synthesis methods described in Section 2.1. In order to obtain value for the uncertainty on the expected detection rates, we place this sample of DCOS in many different Monte Carlo sampled instances of the Milky Way, the model for which is described in Section 2.2. We evolve the orbit of each DCO in a Milky Way instance up to the LISA mission and calculate the detection rate for that instance using the methods presented in Section 2.3.

### 2.1. *Binary population synthesis*

We use the grid of binary population synthesis simulations recently presented in Broekgaarden et al. (2021) and Broekgaarden et al. (in prep). This grid of simulations is synthesised using the rapid population synthesis code COMPAS (Stevenson et al. 2017; Vigna-Gómez et al. 2018; Stevenson et al. 2019). COMPAS follows the approach of the pioneering population synthesis code BSE (Hurley et al. 2000, 2002) and uses fitting formula and rapid algorithms to efficiently predict the final fate of binary systems. The code is open source and documented in the papers listed above, the online documentation[5] and in the upcoming methods paper (Team COMPAS: J. Riley et al. (in prep)). We summarise the main assumptions and settings relevant for this work in Appendix A.

The result of the simulations is a sample of binaries, which, for each metallicity $Z$, have the parameters

$$\mathbf{b}_{Z,i} = \{m_1, m_2, a_{\rm DCO}, e_{\rm DCO}, t_{\rm evolve}, t_{\rm inspiral}, w\}, \quad (1)$$

for $i = 1, 2, \ldots, N_{\rm binary}$, where $m_1$ and $m_2$ are the primary and secondary masses, $a_{\rm DCO}$ and $e_{\rm DCO}$ are the semi-major axis and eccentricity at the moment of double compact object (DCO) formation, $t_{\rm evolve}$ is the time

[5] https://compas.science

between the binary's zero-age main sequence and DCO formation, $t_{\rm inspiral}$ is the time between DCO formation (that is immediately after the second supernova in the system) and gravitational wave merger, $w$ is the adaptive importance sampling weight assigned by STROOPWAFEL (Broekgaarden et al. 2019, Eq. 7). We sample from these sets of parameters when creating synthetic galaxies.

### 2.2. *Galaxy synthesis*

In order to estimate a detection rate of DCOs with statistical uncertainties, we create a series of random instances of the Milky Way, each populated with a subsample drawn (with replacement) from the synthesised binaries described in Section 2.1.

Most previous studies that predict a detection rate for LISA place binaries in the Milky Way independently of their age or evolution. We improve upon this as the first study to use an empirically-informed analytical model of the Milky Way that takes into account the galaxy's enrichment history by applying the metallicity-radius-time relation from Frankel et al. (2018). The authors developed this relation in order to measure the global efficiency of radial migration in the Milky Way and calibrated it using a sample of red clump stars measured with APOGEE (Majewski et al. 2017).

In Section 2.2.1, we outline our model for the Milky Way and in Section 2.2.2 we explain how we combine our population of synthesised DCOs with this Milky Way model.

#### 2.2.1. *Milky Way model*

Our model for the Milky Way accounts for the low-[α/Fe][6] disc, high-[α/Fe] disc and a central component approximating a bar/bulge. The low- and high-[α/Fe] discs are often also referred to as the thin and thick discs because the stellar vertical distribution is better fit by a double exponential rather than a single one. However, it doesn't allow one to assign a star to either the thin or thick disk purely based on its height above the Galactic plane. Therefore, we use the chemical definition of the two disks with the [α/Fe] nomenclature because there is a clear bimodal distribution in the chemical plane, allowing stars to be easily assigned to each of the disc components based on its chemical abundances. For each of the three components, we use a separate star formation history, radial and vertical distribution, which we combine into a single model, weighting each component by its stellar mass. Licquia & Newman (2015) gives that the stellar mass of the bulge is $0.9 \times 10^{10}\,{\rm M}_\odot$ and the stellar mass of the disc is $5.2 \times 10^{10}\,{\rm M}_\odot$, which we split equally between the low- and high-[α/Fe] discs (e.g., Snaith et al. 2014).

*Star formation history:* We use an exponentially declining star formation history (Frankel et al. 2018) (a priori inspired by average the cosmic star formation history) for the combined low- and high-[α/Fe] discs, where the two discs transition at about 8 Gyr ago, and renormalize the produced mass to be equal in each of the two components.

$$p(\tau) \propto \exp\left(-\frac{(\tau_m - \tau)}{\tau_{\rm SFR}}\right), \tag{2}$$

where $\tau$ is the lookback time (the amount of time elapsed between the binary's zero-age main sequence and today), $\tau_m = 12\,{\rm Gyr}$ is the assumed age of the Milky Way and $\tau_{\rm SFR} = 6.8\,{\rm Gyr}$ is the star formation timescale.

The star formation history of the Milky Way bulge (which we assume here to be dominated by the central bar) has many uncertainties due to (1) sizeable age measurement uncertainties at large ages in observational studies, (2) complex selection processes affecting the observed age distributions, and (3) formation mechanisms still under debate. But the central bar was shown to contain stars with an extended age range, with most observed stars between 6 and 12 Gyr (e.g., Bovy et al. 2019), and a younger tail of ages that could come from the subsequent secular growth of the Galactic bar. To model the bar's age distribution more realistically than in previous studies (which assume an old bulge coming from a single starburst), we choose to adopt a more extended star formation history using a $\beta(2, 3)$ distribution, shifted and scaled such that stars are only formed in the range $[6, 12]\,{\rm Gyr}$. We show these distributions in the first panel in the left half of Fig. 1.

*Radial distribution:* For each of the three components we employ the same single exponential distribution (but with different scale lengths)

$$p(R) = \exp\left(-\frac{R}{R_d}\right)\frac{R}{R_d^2}, \tag{3}$$

where $R$ is the Galactocentric radius and $R_d$ is the scale length of the component. For the low-[α/Fe] disc, we set $R_d = R_{\rm exp}(\tau)$, where $R_{\rm exp}(\tau)$ is the scale length presented in Frankel et al. (2018, Eq. 5)

$$R_{\rm exp}(\tau) = 4\,{\rm kpc}\left(1 - \alpha_{R_{\rm exp}}\left(\frac{\tau}{8\,{\rm Gyr}}\right)\right), \tag{4}$$

[6] nomenclature used to describe the enhancement of $\alpha$ elements compared to iron in stellar atmospheres

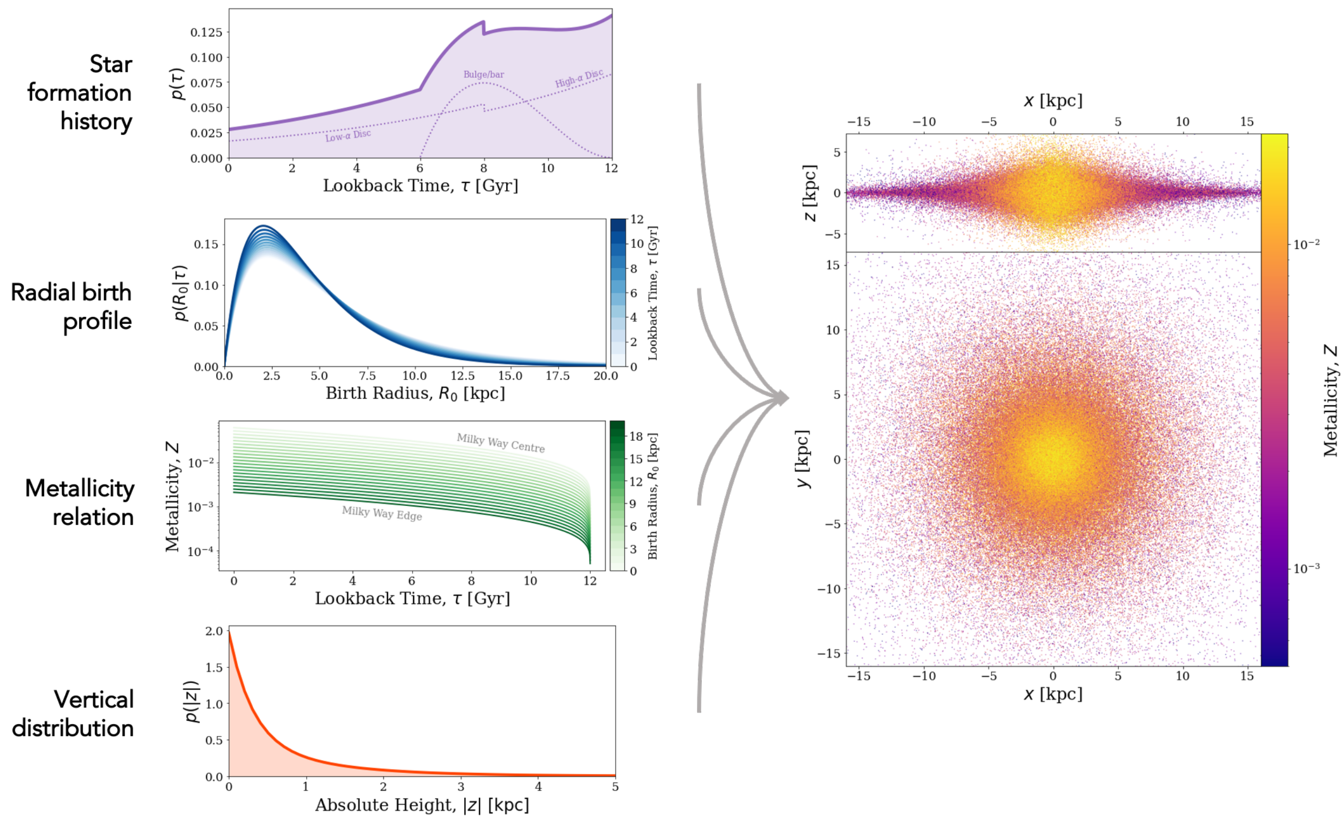


**Figure 1.** A schematic illustrating how we create a mock Milky Way galaxy. The left panel illustrates the different model aspects: star formation history of 3 galactic components (individually shown in the dotted lines), spatial distribution at birth, age-metallicity-radius relation, and vertical distribution. On the right, we show an example instance of the Milky Way with 250000 binaries shown as points colour coded by metallicity. The top panel shows a side-on view and the bottom panel shows a face-on view.

where $\alpha_{R_{\rm exp}} = 0.3$ is the inside-out growth parameter[7]. This scale length accounts for the inside-out growth of the low-[α/Fe] disc and hence is age dependent. We assume $R_d = (1/0.43)$ kpc for the high-[α/Fe] disc (Bovy et al. 2016, Table 1) and $R_d = 1.5$ kpc for the bar component (Bovy et al. 2019). We show the combination of these distributions in the second panel in the left half of Fig. 1.

*Vertical distribution*: Similar to the radial distribution, we use the same single exponential distribution (but with different scale heights) for each component

$$p(|z|) = \frac{1}{z_d} \exp\left(-\frac{z}{z_d}\right), \tag{5}$$

where $z$ is the height above the Galactic plane and $z_d$ is the scale height. We set $z_d = 0.3$ kpc for the low-[α/Fe] disc (McMillan 2011) and $z_d = 0.95$ kpc for the high-[α/Fe] disc (Bovy et al. 2016). For the bar, we set $z_d = 0.2$ kpc (Wegg et al. 2015). We show the combination of these distributions in the last panel in the left half of Fig. 1.

*Metallicity-radius-time relation:* To account for the chemical enrichment of star forming gas as the Milky Way evolves, we adopt the relation given by (Frankel et al. 2018, Eq. 7)

$$\begin{aligned}[\mathrm{Fe/H}](R,\tau) = {} & F_m + \nabla[\mathrm{Fe/H}]R \\ & - \left(F_m + \nabla[\mathrm{Fe/H}]R^{\rm now}_{[\mathrm{Fe/H}]=0}\right) f(\tau),\end{aligned} \tag{6}$$

where

$$f(\tau) = \left(1 - \frac{\tau}{\tau_m}\right)^{\gamma_{[\mathrm{Fe/H}]}}, \tag{7}$$

$F_m = -1$ dex is the metallicity of the gas at the center of the disc at $\tau = \tau_m$, $\nabla[\mathrm{Fe/H}] = -0.075\,\mathrm{kpc}^{-1}$ is the metallicity gradient, $R^{\rm now}_{[\mathrm{Fe/H}]=0} = 8.7$ kpc is the radius at which the present day metallicity is solar and $\gamma_{[\mathrm{Fe/H}]} = 0.3$ set the time dependence of the chemical enrichment. We can convert this to the representation of metallicity that we use in this paper by applying (e.g Bertelli et al. 1994)

$$\log_{10}(Z) = 0.977[\mathrm{Fe/H}] + \log_{10}(Z_\odot). \tag{8}$$

[7] In $R_{\rm exp}(\tau)$, we use 4 kpc instead of 3 kpc for the 0 Gyr exponential scale-length of the disc as NF finds that it provides a better fit to the original data

Although Frankel et al. (2018) only fit this model for the low-[$\alpha$/Fe] disc, we also use this metallicity-radius-time relation for the high-$\alpha$ disc and the bar, but focusing on the chemical tracks more representative to the inner disc and large ages. Sharma et al. (2020) showed that using a simple continuous model for both the low- and high-[$\alpha$/Fe] discs, the Milky Way abundance distributions could be well reproduced. Empirically, the chemical tracks in the [$\alpha$/Fe]-[Fe/H] plane of the stars in the bulge/bar follow the same track as those of the old stars in the Solar neighbourhood (Bovy et al. 2019, Fig. 7,), which motivates our modelling choice to use the same metallicity-radius-time relation.

Fig. 1 shows the distributions and relations outlined in this section and also displays an example random galaxy drawn using this model.

#### 2.2.2. *Combining population and galaxy synthesis*

For each Milky Way instance, we randomly sample the following set of parameters

$$\mathbf{g}_i = \{\tau, R, Z, z, \theta\} \tag{9}$$

for $i = 1, 2, \ldots, N_{\rm MW}$, where we set $N_{\rm MW} = 2 \times 10^5$, $\tau, R, Z$ and $z$ are defined and sampled using the distribution functions specified in Section 2.2.1, $\theta$ is the polar angle sampled uniformly on $[0, 2\pi)$ and $Z$ is the metallicity. Figure 1 shows an example of a random Milky Way instance created with these distributions. This shows how these distributions translate to positions in the Milky and illustrates the gradient in metallicity over radius.

We match each set of galaxy parameters $\mathbf{g}_i$, to a random set of binary parameters $\mathbf{b}_{Z,i}$, by drawing a set of binary parameters from the closest metallicity bin to the metallicity in $\mathbf{g}_i$.

Each binary is likely to move from its birth orbit. Although all stars in the Galactic disc experience radial migration (Sellwood & Binney 2002; Frankel et al. 2018), double compact objects generally experience stronger dynamical evolution as a result of the effects of both Blaauw kicks (Blaauw 1961) and natal kicks (e.g. Hobbs et al. 2005).

The magnitude of the systemic kicks are typically small compared to the initial circular velocity of a binary at each Galactocentric radius. Therefore, we expect that kicks will not significantly alter the overall distribution of their positions. Given this, and for the sake of computational efficiency, we do not account for the displacement due to systemic kicks in our analysis.

### 2.3. *Gravitational wave detection*

We use the Python package LEGWORK to evolve binaries and calculate their LISA detectability. For a full derivation of the equations given below please see the LEGWORK release paper, Wagg et al. 2021b (in prep), or the documentation.

#### 2.3.1. *Inspiral evolution*

Each binary loses orbital energy to gravitational waves throughout its lifetime. This causes the binary to shrink and circularise over time. In order to assess the detectability of a binary, we need to know its eccentricity and frequency at the time of the LISA mission. For each binary in our simulated Milky Way, we know that the time from DCO formation to today is $\tau - t_{\rm evolve}$ and that the initial eccentricity and semi-major axis are $e_{\rm DCO}$ and $a_{\rm DCO}$. We find the eccentricity of the binary at the start of the LISA mission, $e_{\rm LISA}$, by numerically integrating its time derivative (Peters 1964, Eq. 5.13) given the initial conditions. This can be converted to the semi-major axis at the start of LISA, $a_{\rm LISA}$(Peters 1964, Eq. 5.11), which in turn gives the orbital frequency, $f_{\rm orb,LISA}$, by Kepler's third law.

#### 2.3.2. *Binary detectability*

We define a binary as detectable if its gravitational wave signal has a signal-to-noise ratio of greater than 7 (e.g. Breivik et al. 2020; Korol et al. 2020). The sky-, polarisation- and orientation-averaged signal-to-noise ratio, $\rho$, of an inspiraling binary can be calculated with the following (e.g. Finn & Thorne 2000)

$$\rho^2 = \sum_{n=1}^{\infty} \int_{f_{n,i}}^{f_{n,f}} \frac{h_{c,n}^2}{f_n^2 S_{\rm n}\left(f_n\right)} \, {\rm d}f_n \,, \tag{10}$$

where $n$ is a harmonic of the gravitational wave signal, $f_n = n \cdot f_{\rm orb}$ is the frequency of the $n^{\rm th}$ harmonic of the gravitational wave signal, $f_{\rm orb}$ is the orbital frequency, $S_{\rm n}(f_n)$ is the LISA sensitivity curve at frequency $f_n$ (e.g. Robson et al. 2019) and $h_{c,n}$ is the characteristic strain of the $n^{\rm th}$ harmonic, given by (e.g. Barack & Cutler 2004)

$$h_{c,n}^2 = \frac{2^{5/3}}{3\pi^{4/3}} \frac{(G\mathcal{M}_c)^{5/3}}{c^3 D_L^2} \frac{1}{f_{\rm orb}^{1/3}} \frac{g(n,e)}{nF(e)}, \tag{11}$$

where $D_L$ is the luminosity distance to the source, $f_{\rm orb}$ is the orbital frequency, $g(n,e)$ and $F(e)$ are given in Peters & Mathews (1963) and $\mathcal{M}_c$ is the chirp mass, defined as

$$\mathcal{M}_c = \frac{(m_1 m_2)^{3/5}}{(m_1 + m_2)^{1/5}}. \tag{12}$$

We use LEGWORK to calculate the signal-to-noise ratio for each binary and the package ensures that enough harmonics are computed for each binary such that the error on the gravitational wave luminosity remains below 1%.

#### 2.3.3. *Detection rate calculation*

For each physics variation model and DCO type, we compute the total number of merging DCOs in the Milky Way today, $N_{\rm MW}$, based on the COMPAS simulation. This takes into account the true mass and IMF of the Milky Way since our simulations may each have a slightly different galaxy mass and only ever sample from massive stars rather than the full IMF. For more details see Appendix B.

We determine the fraction of binaries that are detectable in each Milky Way instance by summing the adaptive importance sampling weights of the binaries that have an SNR greater than 7 and dividing by the total weights in the simulation. We multiply this fraction by the total number in the Milky Way to find a detection rate.

$$N_{\rm detect} = \frac{\sum_{i=0}^{N_{\rm detect}} w_i}{\sum_{i=0}^{N_{\rm DCO}} w_i} \cdot N_{\rm MW} \tag{13}$$

We calculate the detection rate by Monte Carlo sampling 2500 Milky Way instances (each containing 200,000 DCOs) for each DCO type and every physics variation in order to obtain values for the uncertainty on the expected detection rate.

## 3. RESULTS I - FIDUCIAL

In this section we present our main results for the detectable LISA DCO population in our fiducial model. We find that on average, a 4-year LISA mission will detect about 36 BHBHs, 33 BHNSs and 8 NSNSs (c.f. Table 2). We first show the distribution of the sources together with the sensitivity curve in Section 3.1, before exploring the parameter distributions for detectable sources in Section 3.2 and the measurement uncertainties in Section. 3.4.

### 3.1. *Distribution on the sensitivity curve*

We show the expected distribution of detectable DCOs together with the LISA sensitivity curve in Figure 2. This shows that the detectable population of these DCOs is concentrated at comparatively lower frequencies than the LISA verification binaries (shown as stars in the top panel). This is expected since producing the same SNR as a BHBH, BHNS or NSNS with a relatively lower mass (circular) WDWD requires a higher frequency. This finding is in agreement with Sesana et al. (2020) and as noted in that work, this could possibly be used to distinguish more massive DCOs from WDWDs probabilistically. There are several other notable features in these distributions. To understand these we overplot reference lines indicating where a circular binary with the average chirp mass ($\langle \mathcal{M}_c \rangle$, annotated in each panel) would reside for a given remaining inspiral time (vertical lines) and a given distance (diagonal lines).

Firstly, we note that the peak of the density distribution coincides with the centre of the Milky Way as expected, since binaries are most likely to be formed towards the centre of the Galaxy. Additionally, we expect that if a population is entirely circular, it should be bounded approximately between the 0.1–30 kpc lines, roughly the minimum and maximum distance to a source in the Milky Way. From inspection of the bottom panels with each individual DCO type we see that this is the true for a large fraction of the population. However, there is a distinct subpopulation of binaries that extend downwards, especially around 2 mHz. This offshoot is composed of eccentric binaries for which the circular distance contours do not apply. For illustrative purposes, we plot the 90% contour of only the *circular* sources in our sample over the density distribution in each of the bottom panels and this subsample is indeed bounded by 0.1–30 kpc the distance lines. We also plot a line of constant distance at 30 kpc for an eccentric binary with $e = 0.98$ to show the different limit for eccentric sources. To further illustrate this point, we show the same plot but with each point coloured by its eccentricity in Fig. 11. Overall, we can see that eccentric sources tend to be located on a slightly different location on the sensitivity curve and so this could perhaps be used help in identifying them.

We plot vertical lines that give the inspiral time for a circular binary with the average chirp mass (annotated in each panel). From these lines we can understand the trend of the density distribution decreasing with increasing frequency. Sources with higher frequencies have shorter inspiral times and thus DCOs will spend less time in these regimes, meaning that more sources are detected at lower frequencies. Note that these inspiral time lines should only be used as guidelines for the population as a whole, as the inspiral time of each individual source will be a function of its mass and eccentricity. It is also evident for each DCO source that the tail of the high frequency sources is more numerous near to the Galactic centre than at short distances. This is simply because there are more sources in the galactic centre and so the chances of 'catching' a binary at high frequency are better.

### 3.2. *Properties of the detectable systems*

In Figure 3, we show the distribution of the individual parameters of the population of detectable binaries and discuss the various features in the following sections.

#### 3.2.1. *Orbital Frequency*

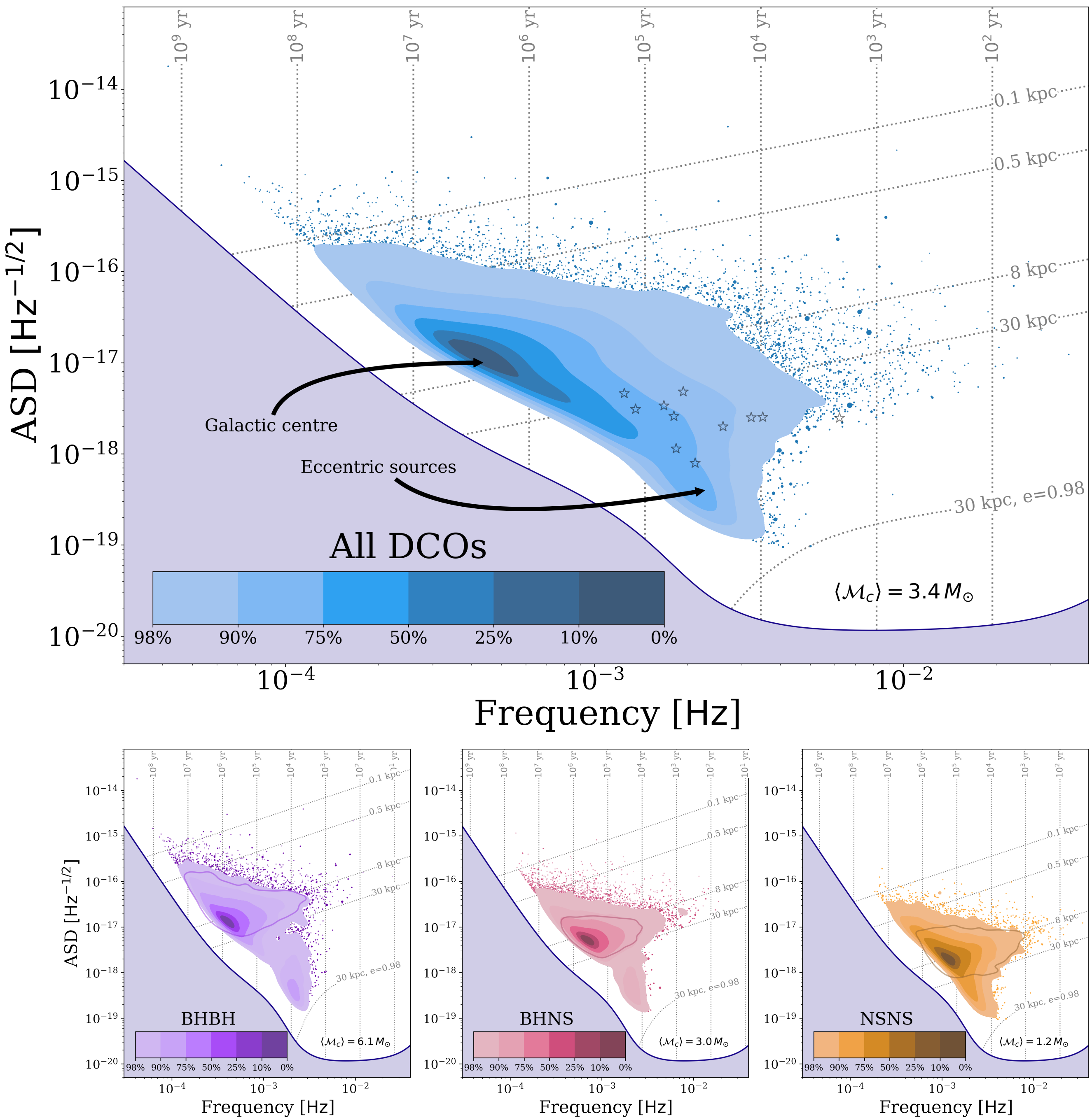


**Figure 2.** Density distribution of detectable BHBH, BHNS and NSNS binaries are shown together with the LISA sensitivity curve. In the top panel we show all systems with the LISA verification binaries over plotted (star symbols, Kupfer et al. 2018). In the bottom panels we separate by type. Contours show the percentage of the population enclosed. The remaining 2% of the population is shown as dots with a size that scales with the sampling weight. For reference we show lines where a circular binary of average chirp mass $\langle \mathcal{M}_c \rangle$ would reside for a given remaining inspiral time (vertical lines) and distance (diagonal line). To highlight the role of eccentricity we further show the signal expected for an eccentric binary at 30 kpc. The coloured line in the bottom panels shows a contour that encloses 90% of the population that is circular. See Sec. 3.1 for a discussion.

The orbital frequency distributions for BHBHs, BHNSs and NSNSs peak at progressively increasing frequencies. This is because a higher mass DCO at the same distance and eccentricity requires a lower frequency to produce the same signal-to-noise ratio and thus be detected. The BHBH distribution has a tail that extends to $8 \times 10^{-6}$ Hz, which is comprised of highly eccentric binaries. These systems are still detectable by LISA as the high eccentricity means that the majority of the GW signal is emitted at higher harmonics at higher frequencies that are located in the LISA band. Similar tails are not as prevalent for BHNSs and NSNSs as they do not have as many eccentric binaries.

#### 3.2.2. *Black Hole Mass*

For both the BHBHs and BHNSs, the black hole mass distribution extends to relatively low masses, with 88% and 90% respectively below $11\,\mathrm{M}_\odot$. Unlike ground-based detectors, LISA is not biased to higher masses and so the mass distribution more closely follows the IMF. In addition, at the high metallicities in the Milky Way, stellar winds are much stronger and strip away much of the stellar mass before BH formation, resulting the less massive black holes. The mass distribution extends down to $2.5\,\mathrm{M}_\odot$, our fiducial maximum neutron star mass. Since the Fryer et al. (2012) *delayed* remnant mass prescription (applied in this work) does not produce a mass gap between neutron stars and black holes. Indeed we expect 35% and 39% of detected BHBH and BHNS systems to contain a black hole in the lower mass gap. Therefore, LISA could help to confirm or rule out the existence of the lower mass gap.

The bimodality of the BHBH distribution is a result of unequal mass ratios. The two peaks are from the primary and secondary black hole masses, which peak around $8\,\mathrm{M}_\odot$ and $3.5\,\mathrm{M}_\odot$ respectively. We show these individual distributions as dotted curves below the main BHBH distribution.

#### 3.2.3. *Mass Ratio*

The mass ratio distribution for each DCO type is relatively distinct from the others. The majority of NSNSs have a mass ratio close to unity, with 90% of systems having $q > 0.8$. The reason for the concentration around equal masses is that most NSs are formed either through electron-capture supernovae or from low mass stars. We set the remnant mass for any system formed through ECSN to $1.26\,\mathrm{M}_\odot$ (see Sec. A.2). The remnant mass prescription that we use gives a fixed fallback mass for any star with a CO core mass less than $2.5\,\mathrm{M}_\odot$, such that many NSs are given the identical mass of $1.278\,\mathrm{M}_\odot$ in the *delayed* prescription (see Fryer et al. 2012, Eq. 19). This means that many NSs are formed with equal masses and hence we see a mass ratio distribution peaked around unity.

In contrast, only 9% of detectable BHBHs are formed with $q > 0.8$ and distribution peaks around $q = 0.4$. The reasoning for these unequal mass ratio systems is as follows: in order to produce a BHBH, most formation channels require at least the first mass transfer to be stable. This stability is strongly dependent on the mass ratio such that equal mass ratios (at the moment of mass transfer) are preferred for creating BHBHs. Yet, since stellar winds are so strong at high metallicity, and even stronger for more massive stars, the primary star will experience significant mass loss and so an initially *unequal* mass ratio is preferred so that the masses are more balanced at the first instance of mass transfer. Since mass transfer occurs after the end of the main sequence for most of our BHBHs, the star will have a well defined core and these core masses, which go on to form BHs, will reflect the initially unequal mass ratios.

We find that detectable BHNSs have even more unequal mass ratios, such that the distribution is almost entire disjoint from that of NSNSs. Moreover, the mass ratio distribution is bimodal, where the two peaks arise from two distinct formation scenarios. Around two thirds of detectable BHNSs experience at least one common envelope event, whilst the last third are formed through only stable mass transfer. The first peak at $q = 0.18$ is from systems that experience at least one CE and occurs at the expected mass ratio, which approximately follows the mean BH mass ($\sim 6.5\,\mathrm{M}_\odot$) and NS mass ($\sim 1.2\,\mathrm{M}_\odot$). Yet we also see a second peak at higher mass ratios around $q = 0.34$, which arise from the fraction of the population that underwent only stable mass transfer. The stability of mass transfer is strongly dependent on the mass ratio and thus these systems have a bias for more equal mass ratio systems, leading to a peak at higher $q$.

#### 3.2.4. *Eccentricity*

The eccentricity distributions show that detectable BHBHs are most likely to be highly eccentric of the three DCOs. This may seem counter-intuitive since neutron stars receive stronger natal kicks, which cause the orbit to become eccentric. However, these stronger kicks often result in disrupted or too-wide binaries in the more weakly bound NSNSs. In contrast, BHBHs can receive strong kicks that impart high eccentricity without disrupting and thus tend to be more eccentric. This effect is compounded by the fact that we can see BHBHs at lower orbital frequencies, meaning that they have not had as much time to circularise and so still have significant eccentricity by the time of the LISA mission.

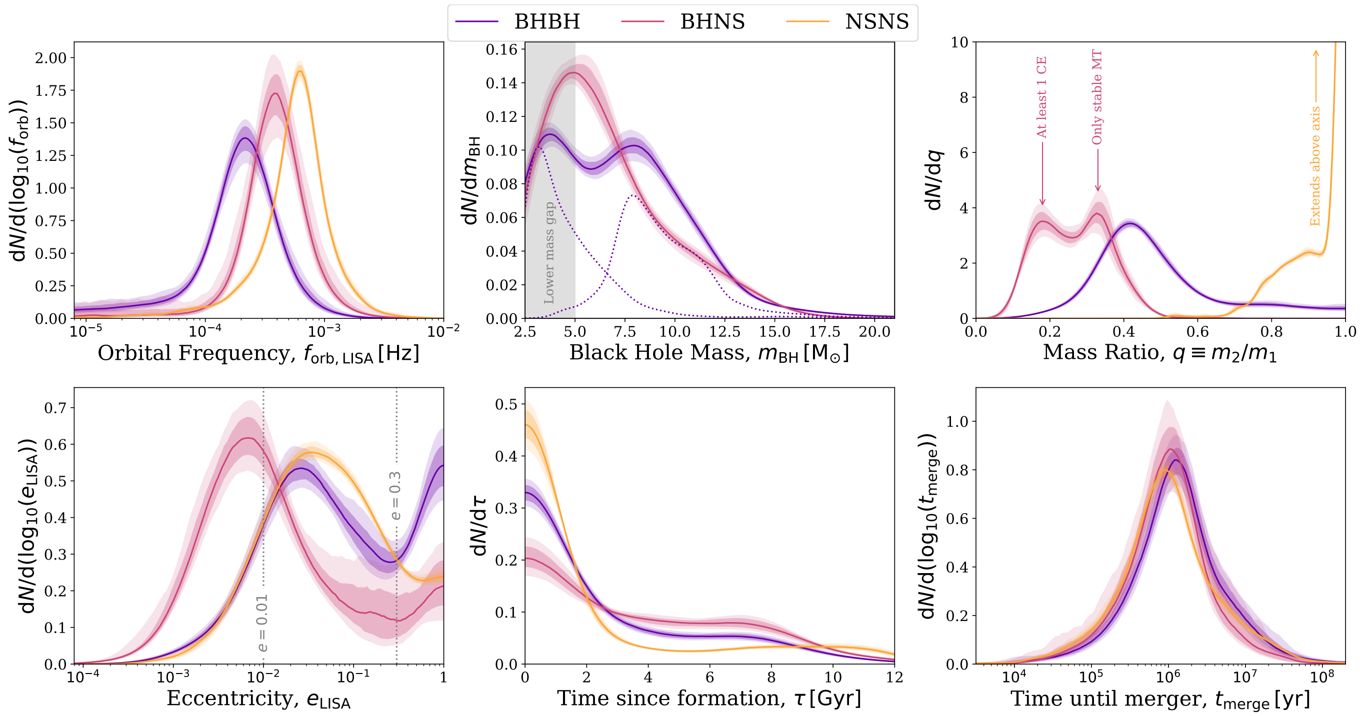


**Figure 3.** Properties of detectable systems for a 4-year LISA mission in our fiducial model. Each panel shows a kernel density estimator for a single property, coloured by DCO type. The shaded areas show the 1- and 2-$\sigma$ uncertainties (obtained via bootstrapping). The dotted lines in the black hole mass panel show the individual primary and secondary mass distributions. See Sec. 3.2 for a discussion.

An eccentricity of $e = 0.01$ is the lower bound on the measurable eccentricity with LISA proposed by Nishizawa et al. (2016). We find that a significant fraction of DCOs (86% of BHBHs, 46% of BHNSs and 86% of NSNSs) exceed this bound. This is in contrast to several previous work that assume all DCOs are circular once they reach the LISA mission (e.g. Lamberts et al. 2018; Sesana et al. 2020). Moreover, we find that 20%, 8% and 12% of BHBHs, BHNSs and NSNSs respectively have $e > 0.3$. At this eccentricity the majority of the gravitational wave power is emitted in higher harmonics above the orbital frequency and thus the signal would appear at higher frequencies in LISA.

#### 3.2.5. *Time since formation*

The progenitors of Galactic DCOs in our sample are formed throughout the history of the Milky Way, with more formed at earlier times (see Fig. 1). In contrast, we find that the *detectable* systems are primarily formed recently, with the majority formed in the past 2 Gyr, in addition to a tail of systems out to earlier times.

The peak at recent times is due to the fact that most binaries in our sample are formed with merger times on the order of a couple of Gyr (since most form through a common envelope phase that significantly tightens the binary). For a binary to be in the LISA band and detectable it must be near the end of its inspiral and so LISA will be most sensitive to sources that were formed a couple of Gyr ago.

The peak is sharpest for NSNSs as they have the highest orbital frequencies and largest fraction of eccentric system, which result in shorter inspiral times and therefore later formation times. Conversely, the peak is less prominent for BHNSs as they are the most circular, have moderate orbital frequencies and masses.

#### 3.2.6. *Time until merger*

The final panel of Fig. 3 shows the remaining time until merger for each of the DCO types at the start of LISA mission. The distributions are strikingly similar and peak with merger times of around a Myr.

The merger time is a function of the mass, frequency and eccentricity of the sources, such that more massive, higher frequency and more eccentric sources merge faster (Peters 1964, Eq. 5.14). So, despite the fact that each DCO type often has higher values in any one of these properties, the convolution of all three tends to negate the differences. For example, NSNSs have the highest orbital frequencies and are mildly eccentric whilst BHNSs have moderate orbital frequencies and are more circular. However, BHNSs are more massive in general and so the overall merger times are distributed very similarly for both DCO types.

### 3.3. *Distribution in the Milky Way*

In the first panel of Fig. 4 we show the distribution of the luminosity distance of detectable systems. Each DCO's luminosity distance distribution peaks around 8 kpc since this is the distance to the centre of the Milky Way and thus the most dense location of DCOs. There is a bias in each distribution for systems at lower distances since closer binaries are easier to detect. This bias is most prominent for the NSNS distribution since, on average, their lower relative masses require a smaller distance in order to be detected.

However, more surprisingly, we also see that the NSNS distribution extends to higher distances than the other DCOs. The reason for this is that the NSNS population has the highest fraction of "mildly" eccentric systems ($0.01 < e < 0.3$). The BHNS population has a much higher fraction of effectively circular systems ($e < 0.01$), which emit weaker gravitational wave compared to equivalent eccentric systems. Therefore, despite their relatively higher masses, the maximum distance at which a source is detectable is generally lower than the eccentric NSNSs and hence the distribution tends to zero at smaller distances. Conversely, the BHBH population has a higher fraction of *high* eccentricity systems $e > 0.3$. Although one may naively expect that this would result in stronger signals (and so further distances), for a system to have these high eccentricities in LISA, it must still be early in its evolution and thus have a low orbital frequencies. The result of this is that high eccentricity systems tend to have lower SNRs and so cannot be detected at large distances. Overall we see that the eccentricity distribution of NSNSs occupies a "sweet spot" where the gravitational wave power is increased compared to circular systems, but it isn't too high that the frequency is significantly impacted. This means that NSNSs can be seen out to the largest distances of the three DCO types.

[TODO: There will also be a little bit more text to explain the example distribution over galaxies in the lower panel – will make properly once Floor combines the latest fiducial simulation data (this plot is sampling uniformly rather than based on the distribution)]

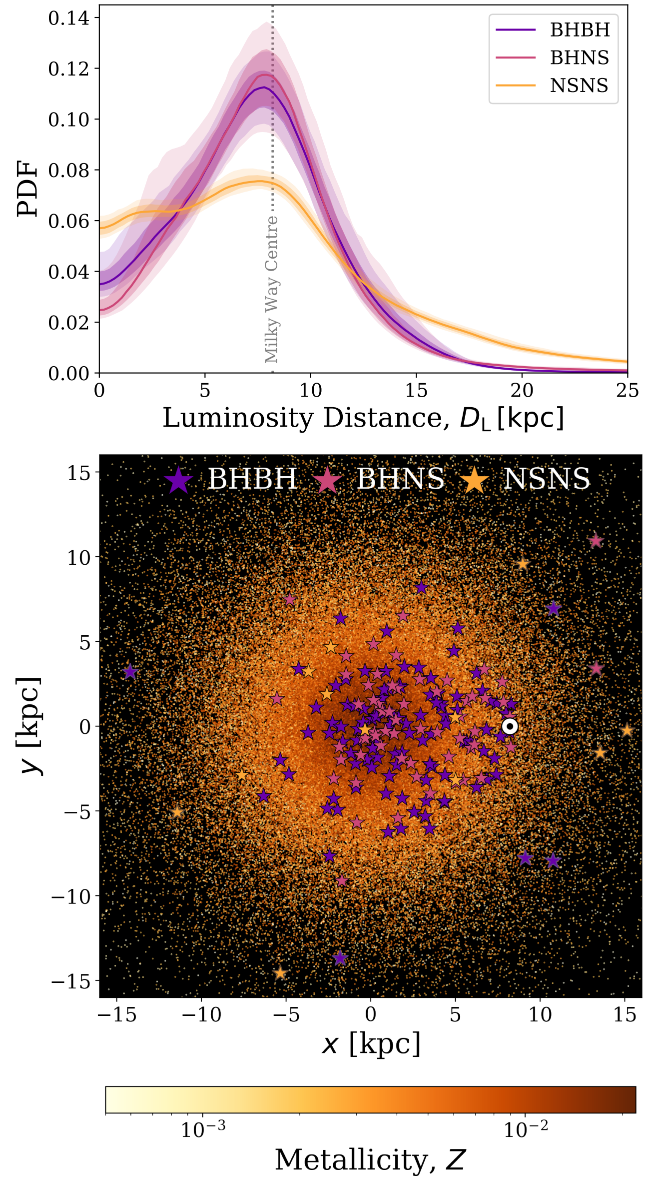


**Figure 4. Top:** As Figure 3, but for the luminosity distance. **Bottom:** A face-on view of an example Milky Way galaxy, where each point is coloured by its metallicity. The large ⊙ shows the position of the Sun. Stars represent a typical example of the detectable systems in a 4-year LISA mission. [TODO: make proper plot, maybe separate panels for different types (hard to arange then though), thoughts on black background?]

### 3.4. *Measurement Uncertainties*

Although it is useful to investigate the underlying parameters of the detectable population, it is also important to consider what LISA will actually *measure* during a detection.

#### 3.4.1. *Chirp mass uncertainty*

The chirp mass uncertainty is important for identifying the source of a GW signal. It is calculated using the uncertainty on the orbital frequency, the time derivative of the orbital frequency and the eccentricity. This is because the chirp mass can be written as

$$\mathcal{M}_c = \frac{c^3}{G}\left(\frac{5\pi}{48n}\frac{\dot{f}_n}{F(e)}\right)^{3/5}\frac{1}{(2\pi f_{\rm orb})^{11/5}}, \qquad (14)$$

where $f_{\rm orb}$ is the orbital frequency, $\mathcal{M}_c$ is the chirp mass (defined in Eq. 12), $e$ is the eccentricity and

$$F(e) = \frac{1 + \frac{73}{24}e^2 + \frac{37}{96}e^4}{(1-e^2)^{7/2}}, \tag{15}$$

is the enhancement factor of gravitational wave emission for an eccentric binary over an otherwise identical circular binary (Peters & Mathews 1963, Eq. 17). Therefore the chirp mass uncertainty is

$$\left(\frac{\Delta\mathcal{M}_c}{\mathcal{M}_c}\right)^2 = \left(\frac{11}{5}\frac{\Delta f_{\rm orb}}{f_{\rm orb}}\right)^2 + \left(\frac{3}{5}\frac{\Delta \dot{f}_{\rm dom}}{\dot{f}_{\rm dom}}\right)^2 + \left(\frac{3}{5}\frac{\Delta F(e)}{F(e)}\right)^2, \tag{16}$$

where $f_{\rm dom}$ is the harmonic frequency with the strongest SNR ($f_{\rm dom} = n_{\rm dom} f_{\rm orb}$ and $n_{\rm dom} = 2$ for circular binaries) as this will provide the best measurement.

We calculate the frequency uncertainties using Takahashi & Seto (2002), such that

$$\frac{\Delta f_{\rm orb}}{f_{\rm orb}} = 4\sqrt{3}\cdot\frac{1}{\rho}\frac{1}{T_{\rm obs}}\frac{1}{f_{\rm orb}}, \tag{17}$$

$$\frac{\Delta \dot{f}_{\rm dom}}{\dot{f}_{\rm dom}} = 6\sqrt{5}\cdot\frac{1}{\rho}\left(\frac{1}{T_{\rm obs}}\right)^2\frac{1}{\dot{f}_{\rm dom}}, \tag{18}$$

where $\rho$ is the signal-to-noise ratio and $T_{\rm obs}$ is the LISA mission length. We calculate the eccentricity certainty, $\Delta e$, following the methods of Lau et al. (2020) and Korol & Safarzadeh (2021), which use the relative SNRs of different harmonics to work out the eccentricity. We propagate this uncertainty such that

$$\frac{\Delta F(e)}{F(e)} = \Delta e \cdot \frac{(1256 + 1608e^2 + 111e^4)e}{96 + 196e^2 - 255e^4 - 37e^6}. \tag{19}$$

We use Eq. 16 to calculate the chirp mass uncertainty for each DCO in our sample and plot it in Fig. 5. We find that approximately 10 BHBHs, 10 BHNSs and 5 NSNSs have measurable chirp masses (as indicated by the shaded region). This uncertainty is generally dominated by the uncertainty on the time derivative of the frequency, since most of the binaries are too early in their inspiral for LISA to measure a strong chirp.

### 3.4.2. *Sky localisation*

We quantify the sky localisation of a source by calculating its angular resolution. Since we find that all potential sources are stationary on the timescale of the LISA mission, following Mandel et al. (2018), we can use the timing accuracy of LISA and the effective detector baseline to calculate the angular resolution, $\sigma_\theta$, as

$$\sigma_\theta = 16.6^\circ \left(\frac{7}{\rho}\right)\left(\frac{5\times10^{-4}\,\rm Hz}{f_{\rm dom}}\right)\left(\frac{2\,\rm AU}{L}\right), \tag{20}$$

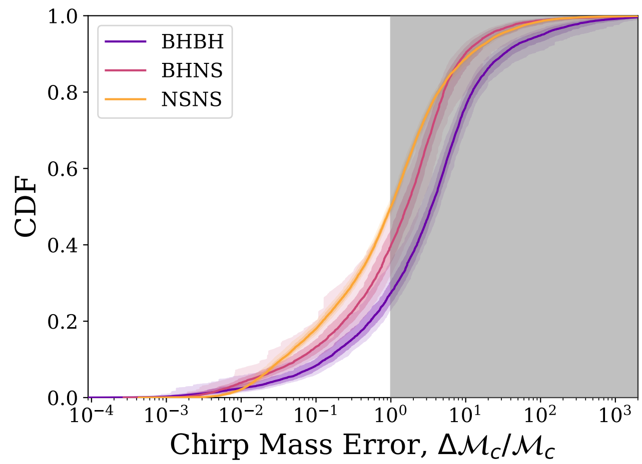


**Figure 5.** Cumulative distribution function for error on the chirp mass. Colours indicate DCO type and shading shows 1- and 2-$\sigma$ uncertainties (obtained via bootstrapping). Shaded region indicates region with unmeasureable chirp mass.

where $L$ is the effective detector baseline, which for LISA is 2 AU since it will orbit the Sun.

We plot the angular resolution in Fig. 6. The area of a patch on the sky that can be attributed to a source is given by $A = \pi\sigma_\theta^2$. From this plot, we see that the majority of sources can be resolved to an angular resolution of 10 degrees. The size of a pencil beam for a 15m diameter SKA dish observing at 1.4 GHz is roughly 0.67 square degrees, corresponding to an angular resolution of $\sigma_\theta = \sqrt{(0.67/\pi)} = 0.46^\circ$ (which, for intuition, is approximately the angular size of the moon). Applying this to the plot shows that about 10-20% of DCOs can be covered by a single pointing of SKA. However, since these LISA sources are essentially stationary in frequency space, observations need not be limited to a single pointing. We will discuss the prospects of matching LISA detections to radio pulsars with SKA further in Sec. 5.2.

## 4. RESULTS II - MODEL VARIATIONS

In this section we explore the effect of varying the underlying binary physics assumptions and the model for the Milky Way. In Section 4.1 we explore the changes in the detection rate over different physics variations and in Section 4.2 we consider how these model physics variations change the properties of detectable systems. Finally we demonstrate how different models for the Milky Way can affect our results in Section C.

### 4.1. *Detection rates*

[Tom: I will be updating this section once the other physics variations are done running. There will be a

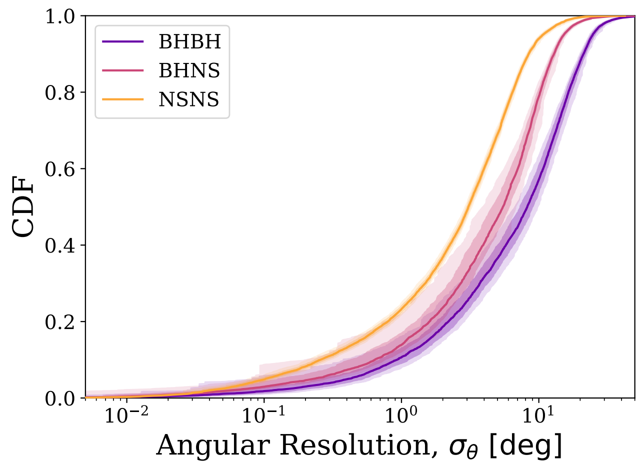


**Figure 6.** As Fig. 5, but for the angular resolution.

couple of new models and the current ones will have better high Z resolution.]

We find that for our fiducial model on average, a 4-year LISA mission will detect 36 BHBHs, 33 BHNSs and 8 NSNSs. Increasing to a 10-year LISA mission length changes the number of detections to 56, 55 and 13 respectively. In Figure 7, we show the expected number of LISA detections for each model variation and discuss the prominent trends in the following sections. We show the rates and uncertainties plotted in this figure in Table 2.

#### 4.1.1. *BHBH detection rate trends*

The BHBH detection rate is markedly robust across physics variations, with the expected detections in each model staying within 25% of the fiducial rate (with the exception of model K). Thus even if there are changes in our understanding of the underlying physics before the LISA mission commences, the expected BHBH detection rate is unlikely to change significantly.

The exception to this statement is model K, in which we allow Hertzsprung gap donors to survive common envelope events. A large fraction of the progenitors of BHs in this mass range expand significantly during the Hertzsprung gap phase and initiate common envelope events. Therefore, though the detectable fraction does not change significantly, the increased population of BHBHs in the Milky Way leads to this model predicting 2.5 times more detections.

#### 4.1.2. *BHNS detection rate trends*

In contrast, the BHNS detection rate is very sensitive to changes in binary physics assumptions. Therefore, once LISA flies and we know the actual number of detections, we can compare to each model and possibly provide some constraint on binary evolution physics. There are several notable trends in the BHNS detection rate in the middle pane of Figure 7.

As $\beta$ increases in models B-D, the BHNS detection rate steadily decreases. This may seem unintuitive since a higher mass transfer efficiency should lead to more massive compact objects and thus a more detectable population. However, one must also consider that most of these DCOs are formed through a common envelope event and so retaining more of the envelope during mass transfer means that the eventual ejection of the envelope is much more difficult, thus leading to more stellar mergers and fewer detectable BHNSs (e.g. Kruckow et al. 2018).

[Tom: @ALL, the trend with common envelopes still confuses me, specifically, why does it not increase when $\alpha = 2.0$? We never quite resolved this in the thread in zpro_tom_wagg with me and Lieke. I do see that the BHBH have a lot of only stable mass transfer and so reasonably are not too affected. NSNS basically only come through CE events and so sensibly are strongly affected but BHNS have $\sim 70\%$ classic channel and so should be affected strongly. But we don't see an increase with $\alpha = 2.0$. Any thoughts? (I'm leaving thinking about this for now in case it changes with the new data haha)]

Enforcing that case BB mass transfer is always unstable (model E) decreases the detection rate as fewer NSs are produced and thus fewer BHNSs form. This is explained in further detail in Section 4.1.3. For the same reason as the BHBH rate, model K has a higher number of detections. This change is less prominent than in the BHBH case as the progenitors tend to be lower masses and initiate a CE event less frequently during the Hertzsprung gap phase.

The Fryer *rapid* prescription (model L) leads to a higher detection rate for BHNSs because progenitors that would become black holes in the *delayed* prescription, instead become neutron stars and so more BHNSs are formed instead of BHBHs. For the same reason, increasing the maximum neutron star mass (model N) increases the detection rate and the inverse is true when it is decreased (model M).

Finally, models P-R show increased detection rates since lower kicks result in fewer disrupted binaries and hence a more numerous detectable population. Following this logic it makes sense that model Q produces more detections than model P. The model with no BH kick (R) is slightly lower than model Q as the number of surviving binaries is limited by the neutron star kick more than the black hole kick.

#### 4.1.3. *NSNS detection rate trends*

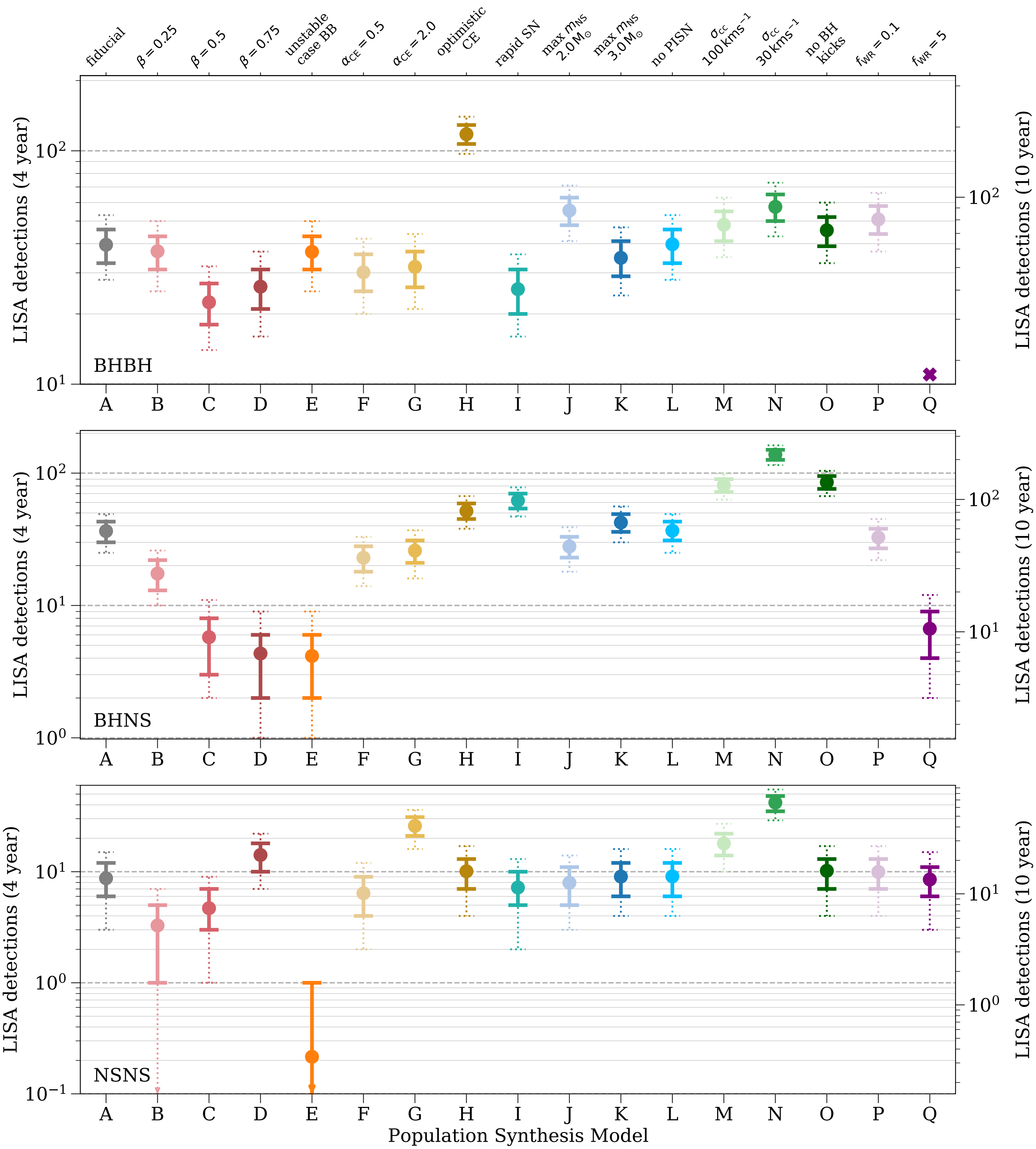


**Figure 7.** The number of expected detections in the LISA mission for different DCO types and model variations. Error bars show the 1- (solid) and 2-$\sigma$ (dotted) Poisson uncertainties. An arrow indicates that the error bar extends to zero. The left axis and grid lines show the number of detections in a 4-year LISA mission and the right axis shows an approximation of the number of detections in a 10-year mission (we scale the axis by $\sqrt{T_{\rm obs}}$, see Table 2 for exact rates). Each model is described in further detail in Table 1 and details of the fiducial assumptions are in Section A.2. See Sec. 4.1 for a discussion. [TODO: subject to change with the updated/new models and new uncertainty estimates]

As $\beta$ increases the NSNS detection rate increases, the opposite trend to that seen in the BHNS rate. This is for two main reasons: firstly the ejection of a common envelope is less problematic for the less massive NSNS binaries. Moreover, the increased mass transfer efficiency means that systems that were previously below the mass necessary to become a NS can now accrete enough mass to form a NS. Although the same is true for more massive stars becoming BHs instead of NSs, due to the IMF, there is a net flux of more stars becoming NSs.

There is a drastic decrease in detections for model E by nearly two orders of magnitude. This is because the majority of NSNS binaries are formed through case BB mass transfer and setting this mass transfer to be always unstable results in many of these binaries to merge before they could become NSNSs. As a result the total number of detections decreases, however, interestingly the remaining population represent more massive progenitors (that would not go through case BB mass transfer) and thus is skewed to higher masses and has a *higher* detectable fraction.

The vast majority of NSNSs in our sample are formed through the common envelope channel and thus changing the value of $\alpha_{\rm CE}$ has an effect on the rate. We see that decreasing $\alpha_{\rm CE}$ (model H) leads to a lower rate as there is less energy available to eject the envelope and so more binaries result to stellar mergers rather than NSNSs and similarly we see an inverse trend when increasing $\alpha_{\rm CE}$ (model I).

As we found in the BHNS trends, a lower value for the core-collapse supernova velocity dispersion increases the detection rate in models P and Q, whilst changing the PISN or BH kick prescription (models O and R) of course has no effect on the NSNS population.

### 4.2. *Properties of detectable systems*

[Tom: This will be about how the shapes of the parameter distributions change for the different model variations. I won't detail every variation but I'll point out anything that stands out and leave the rest in the appendix plots.]

## 5. DISCUSSION

### 5.1. *Identification of GW sources*

It is important to note that, though we present predictions for the detection rates of specific DCO types, the nature of the source may not be immediately apparent from the gravitational wave signal.

The population of Galactic WDWDs detectable with LISA will be several orders of magnitude larger than the more massive DCOs on which we focus in this paper (e.g. Korol et al. 2017). It is therefore imperative that we consider how to distinguish NS and BH binaries from this much more numerous population of sources. In addition to distinguishing them from WDWDs, we must consider how to discriminate between BHBHs, BHNSs and NSNSs themselves.

#### 5.1.1. *Distinguishing from WDWD population*

The simplest way to check whether a source is a WDWD is to check its chirp mass. The mass of a non-rotating white dwarf cannot be larger than the Chandrasekhar limit of $1.44\,{\rm M_\odot}$ (Chandrasekhar 1931), so we can take the maximum chirp mass of a WDWD to be $\sim 1.25\,{\rm M_\odot}$. Therefore, any DCO with a chirp mass that satisfies $\mathcal{M}_c > 1.25\,{\rm M_\odot} + 2\Delta\mathcal{M}_c$ must not be a WDWD. We find that for the detectable population of a 4(10)-year LISA mission, 17(23)% of BHBHs, 20(24)% of BHNSs and 2.4(2.5)% of NSNSs satisfy this condition. This method is not particularly effective for NSNSs since their average chirp mass, $1.17\,{\rm M_\odot}$, is below the Chandrasekhar limit.

Another discriminator between WDWDs and other DCOs is the eccentricity. WDWDs formed in the disc are thought to be formed through isolated binary formation and have little to no eccentricity (e.g. Nelemans et al. 2001). Therefore, if any system is detected with anything other than one detectable harmonic, this implies that the system is unlikely to be a WDWD. We find that for a 4(10)-year LISA mission, 55(61)% of BHBHs, 27(28)% of BHNSs and 65(69)% of NSNSs are detected with multiple harmonics. Both the absolute percentage and the relative improvement with an extended LISA mission is lower for the BHNSs with respect to other DCOs as we find that these BHNSs are less eccentric on average (see Fig. 3 and discussion in Sec. 3.2).

However, we should also consider that eccentric WDWDs could be formed through dynamical formation in Milky Way globular clusters (e.g. Willems et al. 2007; Kremer et al. 2018). This means that we cannot assume that eccentric binaries are not WDWDs unless they are detected in the Galactic plane. We can use the sky localisation, scale height of the disc and distance to the source to estimate what fraction of eccentric sources can be localised to the Galactic plane. This condition can be written as $\sigma_\theta < \arcsin(z_{\rm plane}/D_L)$ or $D_L < z_{\rm plane}$, where we set the height of the Galactic plane, $z_{\rm plane} = 0.95\,{\rm kpc}$, to the scale height of the high-$\alpha$ disc. We apply this condition to find that the fraction of sources that are eccentric *and* localised within the disc for a 4(10)-year LISA mission are 40(32)% for BHBHs, 24(19)% for BHNSs and 59(51)% for NSNSs[8].

Overall, combining these methods we find that for a 4(10)-year mission, LISA will detect at least 15(22) BHBHs, 10(17) BHNSs and 4(7) NSNSs that are distinguishable from the WDWD population.

#### 5.1.2. *Discriminating between BHBHs, BHNSs and NSNSs*

The problem of discriminating between the BHBH, BHNS and NSNS populations can be more difficult than distinguishing them from WDWDs. For NSNSs, we can follow a similar method to the WDWDs (see Sec. 5.1.1) by applying our knowledge of the maximum mass of a neutron star. Following our fiducial assumption, we can take the maximum mass of a neutron star as $2.5\,\mathrm{M}_\odot$ and thus the maximum chirp mass that a system can attain without one of the components being a black hole is $\mathcal{M}_c = 2.2\,\mathrm{M}_\odot$. For a 4(10)-year LISA mission, the fraction of systems that are above or below this limit by more than $2\Delta\mathcal{M}_c$ is 15(20)% for BHBHs, 12(14)% for BHNSs and 34(40)% of NSNSs, which in terms of absolute detections is 5(11) for BHBHs, 4(7) for BHNSs and 3(5) for NSNSs.

For separating the BHBH and BHNS population one could consider the range of mass ratios that could result in the chirp mass and assume that those that are likely close to unity must be BHBHs. Another possible solution would be the existence of electromagnetic counterparts to the gravitational wave signal. In Section 5.2 we consider the possibility of detecting a pulsar within a BHNS or NSNS system. This could be used to identify the type of the source, however it is unlikely that a large fraction of the population will contain pulsars that are beaming towards the Earth.

One could also consider using the eccentricity or orbital frequency to separate the populations since the distributions are different for each DCO type (see Fig. 3). This method would also pose a challenge as it would likely only rule out some DCO types as the source of the signal rather than provide strong evidence of the exact type.

### 5.2. *Matching LISA detections to pulsars with SKA*

Since the vast majority of the LISA detectable population of DCOs will not merge for many years, the main form of electromagnetic counterpart for the this population is pulsars. Therefore, for this section we focus only on BHNSs and NSNSs since no BHBH system will contain a pulsar. The joint detection of a binary pulsar with LISA and SKA would not only help to constrain the parameters of the binary, but also enable investigation of other compact object physics. A pulsar(PSR)+BH can be provide stringent tests of theories of gravity, in particular the "No-hair theorem" (Keane et al. 2015). Alternatively, an ultrarelativstic PSR+NS system could be used to measure the neutron star equation of state up to an order of magnitude more accurately than other proposed observational constraints (Kyutoku et al. 2019; Thrane et al. 2020).

We estimate on average, a LISA DCO localised with an angular resolution of $\sigma_\theta < 1.3°$ or $0.7°$ (for SKA-1 and SKA-2) will never contain more than one pulsar in its sky localisation region (see Appendix D). Given these estimates, and by considering the last panel of Fig. 3, approximately 10 and 6 (for SKA-1 and SKA-2) DCOs containing NSs will be localised well enough such that, *if* the NS is a pulsar, SKA can unambiguously match it to the radio signal.

If there is more than one pulsar in the region given by the LISA sky localisation, one can compare the measured parameters of the system in LISA and SKA. Both SKA and LISA will measure the orbital frequency to high precision, as well as the time derivative of the frequency and chirp mass to a lesser precision, of each of these systems. Therefore, one could perform a targetted search with SKA that checks the sky location given by LISA and only looking for binary pulsars with orbital frequencies within the errors. If there was *still* more than one possible pulsar one could also check against the chirp mass. In this way, it will be possible to get a joint detection between SKA and LISA even when the sky area implied by the LISA detection contains more than one pulsar.

In order to assess the efficacy of this method, we would need to know the probability that two random binary pulsars would have orbital frequencies and chirp masses close enough that one could not tell which pulsar matches the LISA detection. This would require simulating the SKA population of pulsars with a code such as PSRPOPPy to find the frequency and chirp mass distribution, which is beyond the scope of this paper. However, the uncertainty on the orbital frequency of a binary on the detection threshold ($\rho = 7$) for a 4-year LISA mission is $2.5 \times 10^{-9}$ Hz and $1.0 \times 10^{-9}$ Hz for a 10-year mission (calculated using Eq. 17). Therefore, we expect that SKA could likely isolate the correct binary pulsar to match to a LISA detection even when several are present in the sky localisation region.

[8] Note that although the fractions are smaller for the 10 year mission, the *absolute* number of detections is still greater. The fraction decreases because a 10 year mission detects more 'marginal' sources that are just on the cusp of the detection threshold and these sources have the worst sky localisation and thus cannot be confirmed to lie within the Galactic plane.

### 5.3. *Caveats*

*Population synthesis limitations:* As with any study involving a population synthesis code, our results rely on uncertain stellar and binary physics and the use of approximate fitting formulae. COMPAS uses fitting formulae and approximate prescriptions based on (sometimes limited) grids of detailed models to describe the evolution of binary stars. Much of the underlying physics is uncertain, such as the common envelope evolution and mass transfer physics. We attempt to understand the importance of these assumptions by varying over many different physics assumptions.

*Underlying helium star models:* One major weakness is that the Hurley et al. (2000) fitting formulae for the evolution of helium stars are based on a grid of models from $0.3\,\mathrm{M_\odot}$ to $10\,\mathrm{M_\odot}$, for a single metallicity ($Z = 0.02$) and thus the formulae have no metallicity dependence and are extrapolated for higher masses. A more detailed set of models in this regime could lead to large changes in the evolution of naked helium stars, a common progenitor of DCOs, and thus affect the detection rate of DCOs.

*Limited metallicity range:* Another limitation of the stellar evolution fitting formulae that COMPAS uses is that they are limited to a metallicity range of $10^{-4} \leq Z \leq 0.03$ and should not be extrapolated outside this region. However, in the Milky Way (based on the metallicity relation in Frankel et al. (2018)), the metallicity distribution can extend as far as $10^{-5} \leq Z \leq 0.06$, with a significant fraction of star formation occurring past $Z = 0.03$. Therefore, for our study we had to reassign any metallicities outside of COMPAS' range. We expect that stellar winds will be reduced to such a degree that they are effectively zero for any metallicity below the minimum. Hence we set any metallicity below the minimum, $Z = 10^{-4}$, equal to the $Z = 10^{-4}$. Similarly, DCO formation is less efficient at high metallicity (e.g. Broekgaarden et al. 2021) and so exploring metallicities above the COMPAS maximum is unlikely to contribute significantly to the observed rate. Therefore, we place any sampled metallicity above the maximum of $Z = 0.03$ uniformly randomly in one of the top 5 highest bins (since using a single bin for many binaries leads to unphysical artifacts).

*Other formation channels:* We also note that our findings are only the result of a single formation channel (isolated binary formation). We do not consider other channels such as dynamical formation or chemically homogeneous evolution, which could increase the detection rate and alter the parameter distributions. For instance, Kremer et al. (2018) predict that around 21 systems could be detected in Milky Way globular clusters with LISA, formed through dynamical formation and thus different channels can still contribute significantly to the detection rate.

*Halo and globular clusters:* Our model for the Milky Way, though more extensive than many previous studies, does not consider the contributions from the Galactic halo or globular clusters. Lamberts et al. (2018) found that the halo's contribution to the detection rate was minimal and, since the metallicity distribution of the halo is uncertain, we did not include it in our galaxy model. The impact of globular clusters would have required a more detailed look into dynamical formation that was beyond the scope of this paper but we again highlight the work of Kremer et al. (2018) that investigated these rates.

*Systemic kicks:* We do not include the effect of systemic kicks on the final location of the sources. This would require integrating the orbital evolution of the millions of binaries in our sample and thus was not computationally reasonable to include. We investigated the effect of kicks for a small grid of binaries and found that though they would result in a more spread out distribution within the galaxy (with a smaller concentration in the galaxy centre), the overall distribution of positions would be relatively unchanged and very few sources have strong enough kicks to reach escape velocity for the Milky Way.

*Eccentricity measurement uncertainty:* The method that we use to determine the eccentricity uncertainty is pessimistic as it requires each harmonic to be individually detectable (e.g. Lau et al. 2020). In reality this may not be necessary depending on the efficacy of matched-filter analysis of LISA data. For an eccentric source to have been detected within the LISA data, several harmonics would already have to have been matched as the same source. This could be done by looking in the same region of the sky for signals with similar chirp masses and distances to the most detectable harmonic in order to find other harmonics that are below the regular detection threshold. This would allow one to refine the measurement of the eccentricity uncertainty significantly by comparing the many different harmonics. Therefore, the eccentricity uncertainty that we calculate in this study is a pessimistic estimate. Smaller eccentricity uncertainties would have two main effects on our results. Firstly, the chirp mass error would decrease slightly in the cases where it is dominated by the eccentricity uncertainty. However, it is mainly dominated by the frequency derivative uncertainty since most sources are essentially stationary and so have extremely small chirps. Secondly, it would improve our ability to distinguish between WDWDs and higher mass DCOs. Until we know more about how LISA will search for eccentric sources, we rely upon our pessimistic estimates.

## 6. COMPARISON WITH PREVIOUS STUDIES

In Figure 8, we compare our results to similar previous studies that investigate the population of stellar mass BHBHs, BHNSs and NSNSs that are detectable with LISA. Figure 8 details the expected detection rates predicted by each paper as well as their assumptions regarding their Milky Way galaxy model, binary population synthesis simulation and LISA mission specifications. We only include papers that are similar to our work, such that they use population synthesis and simulate sources in the Galactic plane. Moreover, Figure 8 does not include the numerous papers on the LISA WDWD population as we do not make predictions for these DCOs.

*Nelemans et al. (2001)*—were the first to investigate the population of LISA detectable stellar mass double compact objects. We find a significantly higher detection rate for BHBHs and BHNSs, as well as a slightly lower rate for NSNSs. We can understand this difference from changes both to the specifications of LISA (such as the mission length and SNR threshold for detection) and our understanding of massive star evolution since the publication of their paper, which both strongly affect the expected detections rates.

*Belczynski et al. (2010)*—built upon the work of Nelemans et al. (2001), by using a different population synthesis code with two model variations and a multi-component model for the Milky Way. They find a much lower detection rate for BHNSs and NSNSs (and agreed on zero BHBHs) when compared to Nelemans et al. (2001). They claim that this discrepancy comes from differences in their population synthesis and an overall lower formation rate rather than any changes to LISA detectability. The low total detection rate for all DCOs in this paper compared to our work is unsurprising given the relatively high SNR threshold of 10 and short mission length of 1 year. The reduced mission length means that the source signal has much less time to accumulate, whilst also fewer WDWDs can be resolved in this time, leading to a weaker signal and an increased Galactic confusion noise relative to our work.

*Liu & Zhang (2014)*—performed a similar investigation using a different population synthesis code and find higher rates than earlier works. Their lower detection threshold and longer mission length compared to Belczynski et al. (2010) likely explains the relatively increased rates. Yet their rates are still significantly below what we find. This could be for several reasons; they assume all binaries are circular both in their evolution and for detection. This means that systems may not have inspiralled as far before the LISA mission or may appear to have weaker gravitational waves when eccentricity is not accounted for. They also use a simplified model for the Milky Way with a single disc of one metallicity and constant star formation, whilst also using a mission length half what we assume. Each of these factors likely contributes to the lower overall detection rates.

*Lamberts et al. (2018)*—presented a new approach to the problem by using the FIRE simulation (Hopkins et al. 2014) to distribute their sources rather than an analytical model of the Milky Way, thus being the first paper in this area to incorporate metallicity dependence into their Milky Way model. Sesana et al. (2020) followed up on this paper using the same simulated BHBH population and presented updated results for the number of expected BHBH detections. They find significantly fewer BHBHs than our fiducial model despite using the same SNR threshold and LISA mission length. The discrepancy between the results of Sesana et al. (2020) and those presented in this work could be caused by different treatments of eccentricity. Unlike our work, Sesana et al. (2020) assume that all binaries are circular for the purpose of detection in LISA, which could result in a lower number of detections by missing eccentric binaries that appear as weaker signals when assumed to be circular. This is especially relevant as we find that around 86% of LISA detectable BHBHs are not circular and around 20% have significant eccentricity (see Section 3.2). We also improve upon this work by using a larger number of metallicity bins compared to Sesana et al. (2020), since a low number of metallicity bins can produce artificial features in the mass distribution of DCOs and possibly affect the detection rate (see Section C). Finally, it could be that different implicit assumptions in their population synthesis code lead to differences in our results (Toonen et al. 2014).

*Lau et al. (2020)*—focussed on the number of Galactic NSNS binaries that could be detected by LISA. Their study uses the same population synthesis code, COMPAS, as this work, though an earlier version. Despite this, their study finds a much larger number of detections. They make several different physical assumptions in their population synthesis, using the Fryer et al. (2012) *rapid* remnant mass prescription, limiting the maximum neutron star mass to $2\,\mathrm{M}_\odot$ and not implementing PISN. However, we note that none of these assumptions strongly affect the NSNS LISA detection rate (see bottom panel of Fig. 7, models L, M and O) and

| | | Predicted DCO Detection Rates | | | Population Synthesis | | | |
|---|---|---|---|---|---|---|---|---|
| **Author** | **Year** | **BHBH** | **BHNS** | **NSNS** | **Code** | **Open Source Code** | **Metallicity** | **Binary Physics Variations** |
| ***Wagg*** | ***2021*** | **35.7 56.3** | **32.8 55.1** | **8.4 13.5** | **COMPAS** | ✓ | **50 bins between [1e-4, 3e-2]** | **20** |
| *Breivik* | *2020* | 93 | 33 | 8 | COSMIC | ✓ | 0.02, 0.003 | None |
| *Lau* | *2020* | ✗ | ✗ | 35 | COMPAS | ✓ | 0.0142 | Case BB always unstable, Single SN, alpha=0.1 |
| *Sesana* | *2020* | 4.2 6.5 | ✗ | ✗ | BSE | ✓ | 13 bins between [1e-4, 3e-2] | None |
| *Lamberts* | *2018* | 25 | ✗ | ✗ | BSE | ✓ | 13 bins between [1e-4, 3e-2] | None |
| *Liu* | *2014* | 6 | 3 | 16 | BSE | ✓ | 0.02 | None |
| *Belczynski* | *2010* | 2.3 0 | 0.2 0 | 4 1.7 | Startrack | ✗ | 0.02 (disc, bulge), 0.001 (halo) | Optimistic CE, Pessimistic CE |
| *Nelemans* | *2001* | 0 | 3 | 39 | SeBa | ✗ | 0.02 | None |

| | | Galaxy and Positioning | | | | Detection | | |
|---|---|---|---|---|---|---|---|---|
| **Author** | **Year** | **Star formation history** | **Spatial distribution** | **Galactic Components** | **Metallicity Dependent Distributions** | **SNR Limit** | **LISA Mission Time (yr)** | **Eccentricity Treatment** |
| ***Wagg*** | ***2021*** | **Exponential 8-0 Gyr ago (thin disc), Exponential 12-8 Gyr ago (thick disc), Skewed gaussian 0-6 Gyr (bulge)** | **Exponential radial and vertical, different scale length/height for each component, thin disc has inside-out growth** | **Thin disc, thick disc, bulge** | ✓ | **7** | **4, 10** | **Full** |
| *Breivik* | *2020* | Constant over 10 Gyr (thin disc), 1 Gyr burst 10 Gyr ago (bulge), 1 Gyr burst 11 Gyr (thick disc) | McMillan 2011 | Thin disc, thick disc, bulge | ✗ | 7 | 4 | Full |
| *Lau* | *2020* | Constant | Miyamoto & Nagai potential (disc), Wilkinson & Evans potential (halo) | Single disc or halo | ✗ | 8 | 4 | Full |
| *Sesana* | *2020* | FIRE simulation | FIRE simulation | Everything within 300kpc | ✓ | 7 | 4, 10 | Used for evolution, ignored during detection |
| *Lamberts* | *2018* | FIRE simulation | FIRE simulation | Everything within 300kpc | ✓ | 5 | 4 | Used for evolution, ignored during detection |
| *Liu* | *2014* | Constant over 13.7 Gyr | Exponential radial, sech^2 vertical (Benacquista+2007) | Single disc | ✗ | 7 | 2 | Assumed circular |
| *Belczynski* | *2010* | Constant over 10 Gyr (disc), 1 Gyr burst 10 Gyr ago (bulge), burst at 13 Gyr (halo) | Exponential sphere (bulge), exponential radial and vertical (disc), spherical shell (halo) | Disc, bulge, halo | ✗ | 10 | 1 | Full |
| *Nelemans* | *2001* | Exponential over 10 Gyr | Exponential radial, sech^2 vertical | Single disc | ✗ | 1, 5 | 1 | Full |

**Figure 8.** A table comparing previous studies of a similar nature to this work. The works listed in the table are Nelemans et al. (2001), Belczynski et al. (2010), Liu & Zhang (2014), Lamberts et al. (2018), Sesana et al. (2020), Lau et al. (2020) and Breivik et al. (2020).

so this is unlikely to entirely account for our differences. We therefore surmise that the remaining difference between our results is likely due to way in which we simulate the Milky Way. Lau et al. (2020) use a model for the Milky Way similar to that of Breivik et al. (2020), which we used to estimate how impactful the choice of MW model was in Section C. We find that this simpler model for the Milky Way could result in an overestimate of the NSNS detection rate and so this may explain the discrepancy between our results. Lau et al. (2020) additionally only uses a single metallicity rather than the two used in Breivik et al. (2020) and so this effect could be even stronger.

*Breivik et al. (2020)*—introduced the population synthesis code COSMIC and presented detections for many different DCO types in LISA using this code. They find that LISA will detect 93 BHBH, 33 BHNS and 8 NSNS binaries in the Milky Way over a 4 year mission. They make many different physical assumptions, the most notable being that Breivik et al. (2020) assumes the optimistic CE scenario. Thus it would be more prudent to compare to our results from model K in which we find 118, 52 and 7 detections respectively. Thus the NSNS rate is consistent but we find higher rates for the BHBHs and BHNSs. These differences are likely due to using a different population synthesis code (COSMIC) and using a different model for the Milky Way, particularly the assumptions of two fixed metallicities.

## 7. CONCLUSION & SUMMARY

We provide predictions for the detection rate and population properties of LISA detectable BHBH, BHNS and NSNS. To this end, we use the rapid population synthesis code COMPAS to simulate over two billion massive binaries, to explore the effect of parameters that are varied to represent the most common uncertainties in binary physics. We use an new empirically-informed analytical model to distribute the resulting BHBH, BHNS and NSNS populations in a Milky-Way like galaxy based on their birth metallicity, in order to estimate and investigate the LISA detectable population of BH and NS binaries.

Our main conclusions can be summarised as:

- **Detection rate:** We find that on average, for our fiducial model, a 4(10)-year LISA mission will detect 36(56) BHBHs, 33(55) BHNSs and 8(13) NSNSs.

- **Black hole mass distribution:** We find that the black hole mass distribution for both BHBHs and BHNSs that are detectable with LISA are not skewed towards heavier masses (as in ground-based detectors), with 88% and 91% having masses less than $11\,\mathrm{M}_\odot$ respectively. Moreover, we find that for LISA detectable DCOs, 35% of BHBHs and 39% of BHNSs have masses in the theoretical lower mass gap between NSs and BHs. This implies that LISA will be able provide conclusive evidence about the existence of a lower-mass gap.

- **Eccentricity distribution:** We find that BH and NS binaries still have significant eccentricities when observable by the LISA mission, unlike the more numerous WDWD LISA population. We find that 86(20)% of BHBHs, 46(8)% of BHNSs and 86(12)% of NSNSs have eccentricity of $e > 0.01(0.3)$ at the start of the LISA mission.

- **Physics variations:** For BHBHs, we find that the detection rate is largely unaffected by changes in underlying physics assumptions, except for the optimistic CE scenario and increased Wolf-Rayet winds. Conversely, the BHNS rate varies widely with physics variation, ranging from a mean of 4 to 138. The NSNS shows some variation but only shows large changes under the assumption that case BB mass transfer is unstable and that core-collapse supernovae produce weaker kicks.

- **Distinguishable sources:** For a 4(10)-year LISA mission, we estimate that of the detectable population, at least 15(22) BHBHs, 10(17) BHNSs and 4(7) NSNSs will produce signals that are distinguishable from a signal produced by a WDWD. Additionally, we predict that we will be able to determine whether 5(11) BHBHs, 4(7) BHNSs and 3(5) NSNSs are signals from a binary that contains a black hole.

- **Joint SKA-LISA detections:** We expect that *if* the binary contains a pulsar that is beaming towards Earth, SKA-1 will be able to detect at least 10 LISA DCOs that contain a NS, whilst the increased number of pulsars that could crowd the sky in SKA-2 means that this total decreases to 6. This total could be much higher if we consider that SKA and LISA could match their orbital frequency estimates to select the correct pulsar from a crowded field.

- **Importance of choice of MW model:** Many studies use Milky Way models that use fixed metallicity populations which are assigned irrespective of birth time or position, do not account for the inside-out growth of the thin disc and use constant star formation rates. The use of these simpler MW models may lead to an overestimation of the LISA NSNS detection rate. It may also introduce unphysical artifacts into DCO parameter distributions, particularly the mass distributions, which lead to inaccurate predictions.

*Software:* COMPAS (version 02.12.00) http://github.com/TeamCOMPAS/COMPAS. (Stevenson et al. 2017; Vigna-Gómez et al. 2018; Broekgaarden et al. 2019), `Python` available from python.org, matplotlib (Hunter 2007), `NumPy` (van der Walt et al. 2011), Astropy (http://www.astropy.org Astropy Collaboration et al. 2013, 2018).

ACKNOWLEDGMENTS

We thank Mike Lau, Floris Kummer, Eva Laplace, Rob Farmer, Katie Sharpe, Mathieu Renzo, Katie Brevik, Alberto Sesana, Valeriya Korol, Will Farr, Tyson Littenberg and the members of the COMPAS collaboration for insightful discussions. TW also thanks Terence Lovatt for his advice and help on improving an earlier draft of this project. This project was funded in part by the European Union's Horizon 2020 research and innovation program from the European Research Council (ERC, Grant agreement No. 715063), and by the Netherlands Organization for Scientific Research (NWO) as part of the Vidi research program BinWaves with project number 639.042.728. We further acknowledge the Black Hole Initiative funded by a generous contribution of the John Templeton Foundation and the Gordon and Betty Moore Foundation.

REFERENCES


Abadie, J., Abbott, B. P., Abbott, R., et al. 2010, Classical and Quantum Gravity, 27, 173001, doi: 10.1088/0264-9381/27/17/173001

Abbott, B. P., Abbott, R., Abbott, T. D., et al. 2016, Physical Review X, 6, 041015, doi: 10.1103/PhysRevX.6.041015

—. 2019, Physical Review X, 9, 031040, doi: 10.1103/PhysRevX.9.031040

—. 2020a, ApJL, 892, L3, doi: 10.3847/2041-8213/ab75f5

—. 2017, PhRvL, 119, 161101, doi: 10.1103/PhysRevLett.119.161101

Abbott, R., Abbott, T. D., Abraham, S., et al. 2020b, arXiv e-prints, arXiv:2010.14527. https://arxiv.org/abs/2010.14527

—. 2020c, ApJL, 896, L44, doi: 10.3847/2041-8213/ab960f

—. 2021, ApJL, 913, L7, doi: 10.3847/2041-8213/abe949

Abdul-Masih, M., Banyard, G., Bodensteiner, J., et al. 2020, Nature, 580, E11, doi: 10.1038/s41586-020-2216-x

Abt, H. A. 1983, ARA&A, 21, 343, doi: 10.1146/annurev.aa.21.090183.002015

Amaro-Seoane, P., Audley, H., Babak, S., et al. 2017, arXiv e-prints, arXiv:1702.00786. https://arxiv.org/abs/1702.00786

Antonini, F., & Rasio, F. A. 2016, ApJ, 831, 187, doi: 10.3847/0004-637X/831/2/187

Antonini, F., Toonen, S., & Hamers, A. S. 2017, ApJ, 841, 77, doi: 10.3847/1538-4357/aa6f5e

Astropy Collaboration, Price-Whelan, A. M., Sipőcz, B. M., et al. 2018, AJ, 156, 123, doi: 10.3847/1538-3881/aabc4f

Astropy Collaboration, Robitaille, T. P., Tollerud, E. J., et al. 2013, A&A, 558, A33, doi: 10.1051/0004-6361/201322068

Barack, L., & Cutler, C. 2004, PhRvD, 69, 082005, doi: 10.1103/PhysRevD.69.082005

Bates, S. D., Lorimer, D. R., Rane, A., & Swiggum, J. 2014, MNRAS, 439, 2893, doi: 10.1093/mnras/stu157

Begelman, M. C., Blandford, R. D., & Rees, M. J. 1980, Nature, 287, 307, doi: 10.1038/287307a0

Belczynski, K., Benacquista, M., & Bulik, T. 2010, ApJ, 725, 816, doi: 10.1088/0004-637X/725/1/816

Belczynski, K., Holz, D. E., Bulik, T., & O'Shaughnessy, R. 2016, Nature, 534, 512, doi: 10.1038/nature18322

Belczynski, K., Kalogera, V., Rasio, F. A., et al. 2008, ApJS, 174, 223, doi: 10.1086/521026

Belczynski, K., Taam, R. E., Kalogera, V., Rasio, F. A., & Bulik, T. 2007, ApJ, 662, 504, doi: 10.1086/513562

Bertelli, G., Bressan, A., Chiosi, C., Fagotto, F., & Nasi, E. 1994, A&AS, 106, 275

Blaauw, A. 1961, BAN, 15, 265

Bolton, C. T. 1972, Nature, 235, 271, doi: 10.1038/235271b0

Bovy, J., Leung, H. W., Hunt, J. A. S., et al. 2019, MNRAS, 490, 4740, doi: 10.1093/mnras/stz2891

Bovy, J., Rix, H.-W., Schlafly, E. F., et al. 2016, ApJ, 823, 30, doi: 10.3847/0004-637X/823/1/30

Breivik, K., Coughlin, S., Zevin, M., et al. 2020, ApJ, 898, 71, doi: 10.3847/1538-4357/ab9d85

Breivik, K., Rodriguez, C. L., Larson, S. L., Kalogera, V., & Rasio, F. A. 2016, ApJL, 830, L18, doi: 10.3847/2041-8205/830/1/L18

Broekgaarden, F. S., Berger, E., Neijssel, C. J., et al. 2021, arXiv e-prints, arXiv:2103.02608. https://arxiv.org/abs/2103.02608

Broekgaarden, F. S., Justham, S., de Mink, S. E., et al. 2019, MNRAS, 490, 5228, doi: 10.1093/mnras/stz2558

Chandrasekhar, S. 1931, ApJ, 74, 81, doi: 10.1086/143324

Chattopadhyay, D., Stevenson, S., Hurley, J. R., Bailes, M., & Broekgaarden, F. 2020, arXiv e-prints, arXiv:2011.13503. https://arxiv.org/abs/2011.13503

Corral-Santana, J. M., Casares, J., Muñoz-Darias, T., et al. 2016, A&A, 587, A61, doi: 10.1051/0004-6361/201527130

de Kool, M. 1990, ApJ, 358, 189, doi: 10.1086/168974

de Mink, S. E., & Belczynski, K. 2015, ApJ, 814, 58, doi: 10.1088/0004-637X/814/1/58

de Mink, S. E., Cantiello, M., Langer, N., et al. 2009, A&A, 497, 243, doi: 10.1051/0004-6361/200811439

de Mink, S. E., & Mandel, I. 2016, MNRAS, 460, 3545, doi: 10.1093/mnras/stw1219

Dewi, J. D. M., Pols, O. R., Savonije, G. J., & van den Heuvel, E. P. J. 2002, MNRAS, 331, 1027, doi: 10.1046/j.1365-8711.2002.05257.x

du Buisson, L., Marchant, P., Podsiadlowski, P., et al. 2020, MNRAS, 499, 5941, doi: 10.1093/mnras/staa3225

Eichler, D., Livio, M., Piran, T., & Schramm, D. N. 1989, Nature, 340, 126, doi: 10.1038/340126a0

El-Badry, K., & Quataert, E. 2020, MNRAS, 493, L22, doi: 10.1093/mnrasl/slaa004

Eldridge, J. J., Stanway, E. R., Breivik, K., et al. 2020, MNRAS, 495, 2786, doi: 10.1093/mnras/staa1324

Farmer, R., Renzo, M., de Mink, S. E., Marchant, P., & Justham, S. 2019, ApJ, 887, 53, doi: 10.3847/1538-4357/ab518b

Farr, W. M., Sravan, N., Cantrell, A., et al. 2011, ApJ, 741, 103, doi: 10.1088/0004-637X/741/2/103

Finn, L. S., & Thorne, K. S. 2000, PhRvD, 62, 124021, doi: 10.1103/PhysRevD.62.124021

Frankel, N., Rix, H.-W., Ting, Y.-S., Ness, M., & Hogg, D. W. 2018, ApJ, 865, 96, doi: 10.3847/1538-4357/aadba5

Fryer, C. L., Belczynski, K., Ramirez-Ruiz, E., et al. 2015, ApJ, 812, 24, doi: 10.1088/0004-637X/812/1/24

Fryer, C. L., Belczynski, K., Wiktorowicz, G., et al. 2012, ApJ, 749, 91, doi: 10.1088/0004-637X/749/1/91

Gerosa, D., Ma, S., Wong, K. W. K., et al. 2019, PhRvD, 99, 103004, doi: 10.1103/PhysRevD.99.103004

Gompertz, B. P., Levan, A. J., & Tanvir, N. R. 2020, ApJ, 895, 58, doi: 10.3847/1538-4357/ab8d24

Hamann, W. R., Gräfener, G., Liermann, A., et al. 2019, A&A, 625, A57, doi: 10.1051/0004-6361/201834850

Hamann, W. R., & Koesterke, L. 1998, A&A, 335, 1003

Heuvel, E. P. J. V. D. 2011, Compact stars and the evolution of binary systems (World Scientific Publishing Co. Pte. Ltd), 55–73, doi: 10.1142/9789814374774_0006

Hjellming, M. S., & Webbink, R. F. 1987, ApJ, 318, 794, doi: 10.1086/165412

Hobbs, G., Lorimer, D. R., Lyne, A. G., & Kramer, M. 2005, MNRAS, 360, 974, doi: 10.1111/j.1365-2966.2005.09087.x

Hopkins, P. F., Kereš, D., Oñorbe, J., et al. 2014, MNRAS, 445, 581, doi: 10.1093/mnras/stu1738

Hotokezaka, K., Nissanke, S., Hallinan, G., et al. 2016, ApJ, 831, 190, doi: 10.3847/0004-637X/831/2/190

Hulse, R. A., & Taylor, J. H. 1975, ApJL, 195, L51, doi: 10.1086/181708

Hunter, J. D. 2007, Computing in Science and Engineering, 9, 90, doi: 10.1109/MCSE.2007.55

Hurley, J. R., Pols, O. R., & Tout, C. A. 2000, MNRAS, 315, 543, doi: 10.1046/j.1365-8711.2000.03426.x

Hurley, J. R., Tout, C. A., & Pols, O. R. 2002, MNRAS, 329, 897, doi: 10.1046/j.1365-8711.2002.05038.x

Ivanova, N., Heinke, C. O., Rasio, F. A., Belczynski, K., & Fregeau, J. M. 2008, MNRAS, 386, 553, doi: 10.1111/j.1365-2966.2008.13064.x

Ivanova, N., & Taam, R. E. 2004, ApJ, 601, 1058, doi: 10.1086/380561

Kalogera, V., & Baym, G. 1996, ApJL, 470, L61, doi: 10.1086/310296

Kalogera, V., Belczynski, K., Kim, C., O'Shaughnessy, R., & Willems, B. 2007, PhR, 442, 75, doi: 10.1016/j.physrep.2007.02.008

Keane, E., Bhattacharyya, B., Kramer, M., et al. 2015, in Advancing Astrophysics with the Square Kilometre Array (AASKA14), 40. https://arxiv.org/abs/1501.00056

Klein, A., Barausse, E., Sesana, A., et al. 2016, PhRvD, 93, 024003, doi: 10.1103/PhysRevD.93.024003

Klencki, J., Nelemans, G., Istrate, A. G., & Chruslinska, M. 2021, A&A, 645, A54, doi: 10.1051/0004-6361/202038707

Korol, V., Rossi, E. M., & Barausse, E. 2019, MNRAS, 483, 5518, doi: 10.1093/mnras/sty3440

Korol, V., Rossi, E. M., Groot, P. J., et al. 2017, MNRAS, 470, 1894, doi: 10.1093/mnras/stx1285

Korol, V., & Safarzadeh, M. 2021, MNRAS, 502, 5576, doi: 10.1093/mnras/stab310

Korol, V., Toonen, S., Klein, A., et al. 2020, A&A, 638, A153, doi: 10.1051/0004-6361/202037764

Kreidberg, L., Bailyn, C. D., Farr, W. M., & Kalogera, V. 2012, ApJ, 757, 36, doi: 10.1088/0004-637X/757/1/36

Kremer, K., Chatterjee, S., Breivik, K., et al. 2018, PhRvL, 120, 191103, doi: 10.1103/PhysRevLett.120.191103

Kroupa, P. 2001, MNRAS, 322, 231, doi: 10.1046/j.1365-8711.2001.04022.x

Kruckow, M. U., Tauris, T. M., Langer, N., Kramer, M., & Izzard, R. G. 2018, MNRAS, 481, 1908, doi: 10.1093/mnras/sty2190

Kupfer, T., Korol, V., Shah, S., et al. 2018, MNRAS, 480, 302, doi: 10.1093/mnras/sty1545

Kyutoku, K., Kiuchi, K., Sekiguchi, Y., Shibata, M., & Taniguchi, K. 2018, PhRvD, 97, 023009, doi: 10.1103/PhysRevD.97.023009

Kyutoku, K., Nishino, Y., & Seto, N. 2019, MNRAS, 483, 2615, doi: 10.1093/mnras/sty3322

Lamberts, A., Blunt, S., Littenberg, T. B., et al. 2019, MNRAS, 490, 5888, doi: 10.1093/mnras/stz2834

Lamberts, A., Garrison-Kimmel, S., Hopkins, P. F., et al. 2018, MNRAS, 480, 2704, doi: 10.1093/mnras/sty2035

Lau, M. Y. M., Mandel, I., Vigna-Gómez, A., et al. 2020, MNRAS, 492, 3061, doi: 10.1093/mnras/staa002

Licquia, T. C., & Newman, J. A. 2015, ApJ, 806, 96, doi: 10.1088/0004-637X/806/1/96

Liu, J. 2009, MNRAS, 400, 1850, doi: 10.1111/j.1365-2966.2009.15574.x

Liu, J., Zhang, H., Howard, A. W., et al. 2019, Nature, 575, 618, doi: 10.1038/s41586-019-1766-2

Liu, J., & Zhang, Y. 2014, PASP, 126, 211, doi: 10.1086/675721

Lyne, A. G., & Lorimer, D. R. 1994, Nature, 369, 127, doi: 10.1038/369127a0

Majewski, S. R., Schiavon, R. P., Frinchaboy, P. M., et al. 2017, AJ, 154, 94, doi: 10.3847/1538-3881/aa784d

Manchester, R. N., Hobbs, G. B., Teoh, A., & Hobbs, M. 2005, AJ, 129, 1993, doi: 10.1086/428488

Mandel, I., & Müller, B. 2020, MNRAS, 499, 3214, doi: 10.1093/mnras/staa3043

Mandel, I., Sesana, A., & Vecchio, A. 2018, Classical and Quantum Gravity, 35, 054004, doi: 10.1088/1361-6382/aaa7e0

Marchant, P., Langer, N., Podsiadlowski, P., Tauris, T. M., & Moriya, T. J. 2016, A&A, 588, A50, doi: 10.1051/0004-6361/201628133

Marchant, P., Renzo, M., Farmer, R., et al. 2019, ApJ, 882, 36, doi: 10.3847/1538-4357/ab3426

Margalit, B., & Metzger, B. D. 2017, ApJL, 850, L19, doi: 10.3847/2041-8213/aa991c

Massevitch, A., & Yungelson, L. 1975, Mem. Soc. Astron. Italiana, 46, 217

McKernan, B., Ford, K. E. S., & O'Shaughnessy, R. 2020, MNRAS, 498, 4088, doi: 10.1093/mnras/staa2681

McMillan, P. J. 2011, MNRAS, 414, 2446, doi: 10.1111/j.1365-2966.2011.18564.x

Metzger, B. D. 2017, Living Reviews in Relativity, 20, 3, doi: 10.1007/s41114-017-0006-z

Miller, M. C., & Lauburg, V. M. 2009, ApJ, 692, 917, doi: 10.1088/0004-637X/692/1/917

Miller-Jones, J. C. A., Bahramian, A., Orosz, J. A., et al. 2021, Science, 371, 1046, doi: 10.1126/science.abb3363

Morris, M. 1993, ApJ, 408, 496, doi: 10.1086/172607

Narayan, R., Piran, T., & Shemi, A. 1991, ApJL, 379, L17, doi: 10.1086/186143

Nelemans, G., Yungelson, L. R., & Portegies Zwart, S. F. 2001, A&A, 375, 890, doi: 10.1051/0004-6361:20010683

Nishizawa, A., Berti, E., Klein, A., & Sesana, A. 2016, PhRvD, 94, 064020, doi: 10.1103/PhysRevD.94.064020

Nissanke, S., Vallisneri, M., Nelemans, G., & Prince, T. A. 2012, ApJ, 758, 131, doi: 10.1088/0004-637X/758/2/131

Nomoto, K. 1984, ApJ, 277, 791, doi: 10.1086/161749

—. 1987, ApJ, 322, 206, doi: 10.1086/165716

Öpik, E. 1924, Publications of the Tartu Astrofizica Observatory, 25, 1

Özel, F., Psaltis, D., Narayan, R., & McClintock, J. E. 2010, ApJ, 725, 1918, doi: 10.1088/0004-637X/725/2/1918

Paczyński, B., & Sienkiewicz, R. 1972, AcA, 22, 73

Peters, P. C. 1964, Physical Review, 136, 1224, doi: 10.1103/PhysRev.136.B1224

Peters, P. C., & Mathews, J. 1963, Physical Review, 131, 435, doi: 10.1103/PhysRev.131.435

Pfahl, E., Podsiadlowski, P., & Rappaport, S. 2005, ApJ, 628, 343, doi: 10.1086/430515

Pfahl, E., Rappaport, S., Podsiadlowski, P., & Spruit, H. 2002, ApJ, 574, 364, doi: 10.1086/340794

Podsiadlowski, P., Langer, N., Poelarends, A. J. T., et al. 2004, ApJ, 612, 1044, doi: 10.1086/421713

Pols, O. R., Schröder, K.-P., Hurley, J. R., Tout, C. A., & Eggleton, P. P. 1998, MNRAS, 298, 525, doi: 10.1046/j.1365-8711.1998.01658.x

Portegies Zwart, S. F., & McMillan, S. L. W. 2000, ApJL, 528, L17, doi: 10.1086/312422

Robson, T., Cornish, N. J., & Liu, C. 2019, Classical and Quantum Gravity, 36, 105011, doi: 10.1088/1361-6382/ab1101

Rodriguez, C. L., Amaro-Seoane, P., Chatterjee, S., & Rasio, F. A. 2018, PhRvL, 120, 151101, doi: 10.1103/PhysRevLett.120.151101

Rodriguez, C. L., Morscher, M., Pattabiraman, B., et al. 2015, PhRvL, 115, 051101, doi: 10.1103/PhysRevLett.115.051101

Ruiter, A. J., Belczynski, K., Benacquista, M., Larson, S. L., & Williams, G. 2010, ApJ, 717, 1006, doi: 10.1088/0004-637X/717/2/1006

Sana, H., de Mink, S. E., de Koter, A., et al. 2012, Science, 337, 444, doi: 10.1126/science.1223344

Sellwood, J. A., & Binney, J. J. 2002, MNRAS, 336, 785, doi: 10.1046/j.1365-8711.2002.05806.x

Sesana, A. 2016, PhRvL, 116, 231102, doi: 10.1103/PhysRevLett.116.231102

Sesana, A., Lamberts, A., & Petiteau, A. 2020, MNRAS, 494, L75, doi: 10.1093/mnrasl/slaa039

Sharma, S., Hayden, M. R., & Bland-Hawthorn, J. 2020, arXiv e-prints, arXiv:2005.03646. https://arxiv.org/abs/2005.03646

Shenar, T., Bodensteiner, J., Abdul-Masih, M., et al. 2020, A&A, 639, L6, doi: 10.1051/0004-6361/202038275

Shenar, T., Sablowski, D. P., Hainich, R., et al. 2019, A&A, 627, A151, doi: 10.1051/0004-6361/201935684

Sigurdsson, S., & Hernquist, L. 1993, Nature, 364, 423, doi: 10.1038/364423a0

Silsbee, K., & Tremaine, S. 2017, ApJ, 836, 39, doi: 10.3847/1538-4357/aa5729

Smarr, L. L., & Blandford, R. 1976, ApJ, 207, 574, doi: 10.1086/154524

Snaith, O. N., Haywood, M., Di Matteo, P., et al. 2014, ApJL, 781, L31, doi: 10.1088/2041-8205/781/2/L31

Soberman, G. E., Phinney, E. S., & van den Heuvel, E. P. J. 1997, A&A, 327, 620. https://arxiv.org/abs/astro-ph/9703016

Srinivasan, G. 1989, A&A Rv, 1, 209, doi: 10.1007/BF00873079

Stephan, A. P., Naoz, S., Ghez, A. M., et al. 2016, MNRAS, 460, 3494, doi: 10.1093/mnras/stw1220

Stevenson, S., Sampson, M., Powell, J., et al. 2019, ApJ, 882, 121, doi: 10.3847/1538-4357/ab3981

Stevenson, S., Vigna-Gómez, A., Mandel, I., et al. 2017, Nature Communications, 8, 14906, doi: 10.1038/ncomms14906

Taam, R. E., & Sandquist, E. L. 2000, ARA&A, 38, 113, doi: 10.1146/annurev.astro.38.1.113

Takahashi, R., & Seto, N. 2002, ApJ, 575, 1030, doi: 10.1086/341483

Tauris, T. M., Kramer, M., Freire, P. C. C., et al. 2017, ApJ, 846, 170, doi: 10.3847/1538-4357/aa7e89

Tauris, T. M., Langer, N., Moriya, T. J., et al. 2013, ApJL, 778, L23, doi: 10.1088/2041-8205/778/2/L23

Tauris, T. M., Langer, N., & Podsiadlowski, P. 2015, MNRAS, 451, 2123, doi: 10.1093/mnras/stv990

The LIGO Scientific Collaboration, the Virgo Collaboration, the KAGRA Collaboration, et al. 2021, arXiv e-prints, arXiv:2106.15163. https://arxiv.org/abs/2106.15163

Thrane, E., Osłowski, S., & Lasky, P. D. 2020, MNRAS, 493, 5408, doi: 10.1093/mnras/staa593

Timmes, F. X., Woosley, S. E., & Weaver, T. A. 1996, ApJ, 457, 834, doi: 10.1086/176778

Toonen, S., Claeys, J. S. W., Mennekens, N., & Ruiter, A. J. 2014, A&A, 562, A14, doi: 10.1051/0004-6361/201321576

Toonen, S., Portegies Zwart, S., Hamers, A. S., & Bandopadhyay, D. 2020, A&A, 640, A16, doi: 10.1051/0004-6361/201936835

Tout, C. A., Pols, O. R., Eggleton, P. P., & Han, Z. 1996, MNRAS, 281, 257, doi: 10.1093/mnras/281.1.257

Tutukov, A., & Yungelson, L. 1973, Nauchnye Informatsii, 27, 70

Tutukov, A. V., & Yungelson, L. R. 1993, MNRAS, 260, 675, doi: 10.1093/mnras/260.3.675

van den Heuvel, E. P. J., Portegies Zwart, S. F., & de Mink, S. E. 2017, MNRAS, 471, 4256, doi: 10.1093/mnras/stx1430

van der Walt, S., Colbert, S. C., & Varoquaux, G. 2011, Computing in Science and Engineering, 13, 22, doi: 10.1109/MCSE.2011.37

Vigna-Gómez, A., Neijssel, C. J., Stevenson, S., et al. 2018, MNRAS, 481, 4009, doi: 10.1093/mnras/sty2463

Vink, J. S. 2017, A&A, 607, L8, doi: 10.1051/0004-6361/201731902

Vink, J. S., & de Koter, A. 2005, A&A, 442, 587, doi: 10.1051/0004-6361:20052862

Vink, J. S., de Koter, A., & Lamers, H. J. G. L. M. 2000, A&A, 362, 295. https://arxiv.org/abs/astro-ph/0008183

—. 2001, A&A, 369, 574, doi: 10.1051/0004-6361:20010127

Webbink, R. F. 1984, ApJ, 277, 355, doi: 10.1086/161701

Webster, B. L., & Murdin, P. 1972, Nature, 235, 37, doi: 10.1038/235037a0

Wegg, C., Gerhard, O., & Portail, M. 2015, MNRAS, 450, 4050, doi: 10.1093/mnras/stv745

Willems, B., Kalogera, V., Vecchio, A., et al. 2007, ApJL, 665, L59, doi: 10.1086/521049

Woosley, S. E., Blinnikov, S., & Heger, A. 2007, Nature, 450, 390, doi: 10.1038/nature06333

Xu, X.-J., & Li, X.-D. 2010a, ApJ, 716, 114, doi: 10.1088/0004-637X/716/1/114

—. 2010b, ApJ, 722, 1985, doi: 10.1088/0004-637X/722/2/1985

Yu, S., & Jeffery, C. S. 2010, A&A, 521, A85, doi: 10.1051/0004-6361/201014827

# APPENDIX

## A. POPULATION SYNTHESIS

In this section we summarise the main assumptions and settings that we use when performing population synthesis for this work. For a more general overview of every setting see Broekgaarden et al. (2021).

### A.1. *Initial conditions*

We simulate between 1 and 100 million massive binaries for 50 metallicities equally spaced in log space between $Z \in [0.0001, 0.022]$, where $Z$ is the mass fraction of heavy elements. We simulate more binaries for higher metallicities to account for the lower formation rate of DCOs. These metallicities span the allowed metallicity range for the original fitting formulae on which COMPAS is based (Hurley et al. 2000). This is repeated for 19 physics variations (see Section A.3) and so in total over two billion binaries were simulated.

Each binary is sampled from initial distributions for the primary and secondary masses as well as the separation. The primary mass, that is the mass of the initially more massive star, is restricted to $m_1 \in [5, 150]\,\mathrm{M}_{\odot}$, which spans the range of interest for NS and BH formation in binary systems, and drawn from the Kroupa (2001) initial mass function (IMF), $p(m_1) \propto m_1^{-2.3}$. The secondary mass, $m_2$, is drawn using the initial mass ratio of the binary, $q \equiv m_2/m_1$, which we assume to be uniform on $[0, 1]$, therefore $p(q) = 1$ (consistent e.g. with Sana et al. 2012). We additionally restrict the secondary masses $m_2 \geq 0.1\,\mathrm{M}_{\odot}$, which is approximately the minimum mass for a main sequence star. We assume that the initial separation follows a flat in the log distribution with $p(a_i) \propto 1/a_i$ and $a_i \in [0.01, 1000]$ AU (Öpik 1924; Abt 1983). We assume that all binary orbits are circular at birth to reduce the dimensions of initial parameters. Since we focus on post-interaction binaries which will have circularised after mass transfer this is a reasonable assumption and is likely not critical for predicting detection rates (Hurley et al. 2002; de Mink & Belczynski 2015).

We apply the adaptive importance sampling algorithm STROOPWAFEL (Broekgaarden et al. 2019) to improve the yield of our sample. This algorithm increases the prevalence of target DCOs (BHBHs, BHNSs and NSNSs in this case) in the sample and assigns each a weight, $w$, which represents the probability of drawing it without STROOPWAFEL in effect.

### A.2. *Physical assumptions in our fiducial model*

*Stellar Evolution:* To follow the evolution of massive stars, COMPAS relies on fitting formulae by Hurley et al. (2000) to detailed single star models by Pols et al. (1998). COMPAS models the evolution of stars that lose or gain mass closely following the algorithms originally described in Tout et al. (1996) and Hurley et al. (2002).

*Wind mass loss:* We follow the wind prescription from Belczynski et al. (2008), which was based on results from Monte Carlo radiative transfer simulation of Vink et al. (2000, 2001). We use the wind mass loss rates from Vink et al. (2001) for stars above 12500 K and the rates from Hurley et al. (2000) for cooler stars. Additionally, we use a separate, higher wind mass loss rate for luminous blue variable (LBV) stars, following Belczynski et al. (2008), to mimic observer LBV eruptions for stars with luminosities and effective temperatures above the Humphrey Davidson limit. We use the Wolf-Rayet-like mass loss rate from Hamann & Koesterke (1998) with an additional metallicity scaling from Vink & de Koter (2005) for helium stars and set $f_{\mathrm{WR}} = 1$. See Team COMPAS: J. Riley et al. (in prep), Section 3 for the explicit equations.

*Mass Transfer:* In determining the stability of mass transfer we use the $\zeta$-prescription, which compares the radial response of the star with the response of the Roche lobe radius to the mass transfer (e.g. Hjellming & Webbink 1987). The mass transfer efficiency, $\beta \equiv \Delta M_{\mathrm{acc}}/\Delta M_{\mathrm{don}}$, is defined as the fraction of the mass transferred by the donor that is actually accreted by the accretor. We limit the maximum accretion rate for stars to $\Delta M_{\mathrm{acc}}/\Delta t \leq 10 M_{\mathrm{acc}}/\tau_{\mathrm{KH}}$, where $\tau_{\mathrm{KH}}$ is the Kelvin-Helmholtz timescale of the star (Paczyński & Sienkiewicz 1972; Hurley et al. 2002). The maximum accretion rate for compact objects is limited to the Eddington accretion rate. If more mass than these rates is accreted then we assume that the excess is lost through isotropic re-emission in the vicinity of the accreting star (e.g. Massevitch & Yungelson 1975; Soberman et al. 1997). We assume that all mass transfer from a stripped post-helium-burning-star (case BB) onto a neutron star or black hole is unstable (Tauris et al. 2015).

*Common Envelope:* A common envelope phase follows dynamically unstable mass transfer and we parameterise this using the $\alpha$-$\lambda$ prescription from Webbink (1984) and de Kool (1990). We assume $\alpha = 1$, such that all of the gravitational binding energy is available for the ejection of the envelope. For $\lambda$ we use the fitting formulae from

Xu & Li (2010a,b). We assume that any Hertzsprung gap donor stars that initiate a common envelope phase will not survive this phase due to a lack of a steep density gradient between the core and envelope (Taam & Sandquist 2000; Ivanova & Taam 2004; Klencki et al. 2021). This follows the 'pessimistic' common envelope scenario (c.f. Belczynski et al. 2007). We remove any binaries where the secondary immediately fills its Roche lobe upon the conclusion of the common envelope phase as we treat these as failed common envelope ejections, likely leading to a stellar merger.

*Supernovae:* We draw the remnant masses and natal kick magnitudes from different distributions depending on the type of supernova that occurs. For stars undergoing a general core-collapse supernova, we use the *delayed* supernova remnant mass prescription from Fryer et al. (2012). The *delayed* prescription does not reproduce the neutron star black hole mass gap and we use this as our default as it has been shown to provide a better fit for observed populations of DCOs (e.g. Vigna-Gómez et al. 2018). We draw the natal kick magnitudes from a Maxwellian velocity distribution with a one-dimensional root-mean-square velocity dispersion of $\sigma_{\rm rms}^{\rm 1D} = 265\,{\rm km\,s^{-1}}$ (Lyne & Lorimer 1994; Hobbs et al. 2005). We assume that stars with helium core masses between 1.6–2.25 $\rm M_\odot$ (Hurley et al. 2002) experience electron-capture supernovae (ECSN) (Nomoto 1984, 1987; Ivanova et al. 2008). We set all remnant masses to $1.26\,\rm M_\odot$ in this case as an approximation of the solution to Equation 8 of Timmes et al. (1996). For these supernovae, we set $\sigma_{\rm rms}^{\rm 1D} = 30\,{\rm km\,s^{-1}}$ (e.g. Pfahl et al. 2002; Podsiadlowski et al. 2004). We assume that stars that undergo case BB mass transfer (Dewi et al. 2002) experience extreme stripping which leads to an ultra-stripped supernova (Tauris et al. 2013, 2015). For these supernovae we calculate the remnant mass using the Fryer et al. (2012) prescription and use $\sigma_{\rm rms}^{\rm 1D} = 30\,{\rm km\,s^{-1}}$ (as with ECSN). Stars with final helium core masses between 35-135 $\rm M_\odot$ are presumed to undergo a pair-instability, or pulsational pair-instability supernova (e.g. Woosley et al. 2007; Farmer et al. 2019). We follow the prescription from Marchant et al. (2019) as implemented in (Stevenson et al. 2019) for these supernovae. We assume that kicks are isotropic in the frame of the collapsing star. We adopt a maximum neutron star mass of $2.5\,\rm M_\odot$ (e.g. Kalogera & Baym 1996; Fryer et al. 2015; Margalit & Metzger 2017) for the fiducial model and change the Fryer et al. (2012) prescription accordingly.

### A.3. *Model variations*

In addition to our fiducial model for the formation of DCOs, we explore 19 other models in which we change various aspects of the mass transfer, common envelope, supernova and wind mass loss physics assumptions in order to assess the effect of their uncertainties on the overall double compact object detection rates and distributions. Each of the models varies a single physics assumption (fiducial assumptions are outlined in Section A.2) and these models are outlined in Table 1.

Our fiducial model is labelled model A. Models B-F focus on changes to the mass transfer physics assumptions. We explore the effect of fixing the mass transfer efficiency $\beta$ to a constant value, rather than allowing it to vary based on the maximum accretion rate. In models B, C, D, in which we set the value of $\beta$ to 0.25, 0.5 and 0.75 respectively. In model E we investigate the consequence of assuming that case BB mass transfer onto a neutron star or black hole is always stable rather than always unstable.

Models G-K focus on altering the common envelope physics. We change the common envelope efficiency parameter to $\alpha_{\rm CE} = 0.1, 0.5, 2.0, 10.0$ in models G, H, I and J respectively. In model K, we relax our restriction that Hertzsprung gap donor stars cannot survive common envelope events, thereby following the 'optimistic' common envelope scenario. We combine this with model E in model F.

In models L-R we consider changes related to our assumptions about supernova physics. Model L uses the alternate *rapid* remnant mass prescription from Fryer et al. (2012) instead of the *delayed* prescription. We change the maximum neutron star mass in models M and N to 2 and $3\,\rm M_\odot$ respectively to account for the range of predicted maximum neutron star masses. Model O removes the implementation of pair-instability and pulsational pair-instability supernovae. In models P and Q we decrease the root-mean-square velocity dispersion for core-collapse supernovae to explore the effect of lower kicks. Model R removes the natal kick for all black holes.

Finally, in models S-T we investigate the effect of changing our assumption about wind mass loss rates, specifically for Wolf-Rayet winds. We vary $f_{\rm WR}$ to 0.1 and 5.0 in models S and T respectively. These values approximately span the current range of possible Wolf-Rayet wind efficiencies suggested from observations (e.g. Vink (2017), Hamann et al. (2019), Shenar et al. (2019), Miller-Jones et al. (2021) and van Son et al. (in prep)).

| Model | Physics Variation |
|---|---|
| A | Fiducial (see Section A.2) |
| B | Fixed mass transfer efficiency of $\beta = 0.25$ |
| C | Fixed mass transfer efficiency of $\beta = 0.5$ |
| D | Fixed mass transfer efficiency of $\beta = 0.75$ |
| E | Case BB mass transfer is always unstable |
| F | Model E + Model K |
| G | CE efficiency parameter $\alpha = 0.1$ |
| H | CE efficiency parameter $\alpha = 0.5$ |
| I | CE efficiency parameter $\alpha = 2$ |
| J | CE efficiency parameter $\alpha = 10$ |
| K | HG donor stars initiating a CE survive CE |
| L | Fryer rapid SN remnant mass prescription |
| M | Maximum NS mass is fixed to $2\,\mathrm{M_{odot}}$ |
| N | Maximum NS mass is fixed to $3\,\mathrm{M_{odot}}$ |
| O | PISN and pulsational-PISN not implemented |
| P | $\sigma_{\rm rms}^{\rm 1D} = 100\,\mathrm{km\,s^{-1}}$ for core-collapse supernova |
| Q | $\sigma_{\rm rms}^{\rm 1D} = 30\,\mathrm{km\,s^{-1}}$ for core-collapse supernova |
| R | Black holes receive no natal kick |
| S | Wolf-Rayet wind factor $f_{\rm WR} = 0.1$ |
| T | Wolf-Rayet wind factor $f_{\rm WR} = 5.0$ |

**Table 1.** A description of the 20 binary population synthesis models used in this study. A is the fiducial model, B-F change mass transfer physics, G-K change common envelope physics , L-R change supernova physics and S-T change wind mass loss (c.f. Broekgaarden et al. 2021, Table 2).

## B. DETECTION RATE NORMALISATION

In this section we explain the normalisation process that we refer to in Section 2.3. From each simulated instance of the Milky Way we extract the fraction of targets that are detectable, where we define a target as one of BHBH, BHNS or NSNS that merges in a Hubble time. To convert the detectable fraction to a detection rate for the Milky Way, we write that the *number* of detectable targets in the Milky Way is

$$N_{\rm detect} = f_{\rm detect} \cdot N_{\rm target,MW}, \tag{B1}$$

where $f_{\rm detect}$ is the fraction of targets in the instance that were detectable and $N_{\rm target,MW}$ is the total number of targets that have been formed in the Milky Way's history. We can further break this total down into

$$N_{\rm target,MW} = \langle \mathcal{R}_{\rm target} \rangle \cdot M_{\rm SF,MW}, \tag{B2}$$

where $\langle \mathcal{R}_{\rm target} \rangle$ is the average number of targets formed per star forming mass and $M_{\rm SF,MW}$ is the star forming mass of the Milky Way, meaning the total mass of every star ever formed in the Milky Way.

### B.1. *Average target formation rate*

Double compact object formation is metallicity dependent, so we find the average rate as the integral over metallicity, which is given by

$$\langle \mathcal{R}_{\rm target} \rangle = \int_{Z_{\rm min}}^{Z_{\rm max}} p_Z \mathcal{R}_{\rm target,Z} \, {\rm d}Z \,, \tag{B3}$$

where $Z_{\rm min}, Z_{\rm max}$ are the minimum and maximum sampled metallicities, $p_Z$ is the probability of forming a star at the metallicity $Z$ (which can be found using the distribution in Frankel et al. 2018) and $\mathcal{R}_{\rm target,Z}$ is the number of targets formed per star forming mass,

$$\mathcal{R}_{\rm target,Z} = \frac{N_{\rm target,Z}}{M_{\rm SF,Z}}. \tag{B4}$$

In practice, this integral is instead approximated as a sum over the metallicity bins that we use in our simulation. The number of targets in our sample at a metallicity $Z$, $N_{\rm target,Z}$, can be written simply as the sum of the targets' weights:

$$N_{\rm target,Z} = \sum_{i=1}^{N_{\rm binaries,Z}} w_i \theta_{\rm target,i}, \tag{B5}$$

where $w_i$ is the adaptive importance sampling weight assigned to the binary by STROOPWAFEL, $N_{\rm binaries,Z}$ is the number of binaries at metallicity $Z$ in our sample and $\theta_{\rm target,i}$ is a step function that is only 1 when the binary is a target and otherwise 0.

The total star forming mass at a metallicity $Z$, $M_{\rm SF,Z}$, can be written as

$$M_{\rm SF,Z} = \frac{\langle m \rangle_{\rm COMPAS,Z}}{f_{\rm trunc}} \sum_{i=1}^{N_{\rm binaries,Z}} w_i, \tag{B6}$$

where $\langle m \rangle_{\rm COMPAS}$ is the average star forming mass of a binary in our sample and $f_{\rm trunc}$ is the fraction of the total stellar mass from which COMPAS samples, given its truncated mass and separation ranges (see Section 2.1). These truncations mean that only $f_{\rm trunc} \approx 0.2$ of the stellar mass in the galaxy is sampled from.

### B.2. *Total star forming mass in the Milky Way*

It is important to distinguish between the *total* mass of every star formed over the entire history of the Milky Way and the *current* stellar mass in the Milky Way. Many stars born in the Milky Way are no longer living and have lost much of their mass to stellar winds and supernovae, thus the current stellar mass in the Milky Way is an underestimate of the total star forming mass.

Licquia & Newman (2015) find that the total stellar mass today in the Milky Way is $6.08 \pm 1.14 \times 10^{10}\,\mathrm{M_\odot}$.

This total includes all stars and stellar remnants (white dwarfs, neutrons stars and black holes) but *excludes* brown dwarfs. We can write that the total mass of every star every formed in the Milky Way is

$$M_{\rm SF,MW} = (6.08 \pm 1.14) \times 10^{10}\,{\rm M}_{\odot} \cdot \frac{\langle m \rangle_{\rm SF,total}}{\langle m \rangle_{\rm SF,today}}, \quad \text{(B7)}$$

where $\langle m \rangle_{\rm SF,total}$ is the average mass of a star over the history of the Milky Way and is defined as

$$\langle m \rangle_{\rm SF,total} = \int_0^{t_{\rm MW}} p_{\rm birth}(\tau) \int_{0.01}^{200} \zeta(m)\ m \,{\rm d}m \,{\rm d}\tau\,, \quad \text{(B8)}$$

where $t_{\rm MW}$ is the age of the Milky Way, $\zeta(m)$ is the Kroupa (2001) IMF function and $p_{\rm birth}(\tau)$ is the probability of a star being formed at a lookback time $\tau$ (Eq. 2). $\langle m \rangle_{\rm SF,today}$ is the average mass of all stars and stellar remnants (excluding brown dwarfs) present in the Milky Way today is defined as follows (note that we integrate from 0.08 not 0.01 since observations of today's Milky Way mass exclude brown dwarfs)

$$\langle m \rangle_{\rm SF,today} = \int_0^{t_{\rm MW}} p_{\rm birth}(\tau) \int_{0.08}^{200} \zeta(m)\ m_{\rm today} \,{\rm d}m \,{\rm d}\tau\,, \quad \text{(B9)}$$

where $m_{\rm today}(m, Z, \tau)$ is the current mass of a star that was formed $\tau$ years ago at a metallicity $Z$. We calculate $m_{\rm today}(m, Z, \tau)$ by interpolating the final masses given by COMPAS for a grid of single stars over different masses and metallicities using the Fryer et al. (2012) delayed prescription and default wind mass loss settings. For $Z$, we use the average star forming metallicity in the Milky Way at a lookback time $\tau$ using our galaxy model. Evaluating Equation B7, we find that the total mass of every star that has ever formed in the Milky Way is

$$\begin{aligned} M_{\rm SF,MW} &= (6.1 \pm 1.1) \times 10^{10}\,{\rm M}_{\odot} \cdot \frac{0.378\,{\rm M}_{\odot}}{0.221\,{\rm M}_{\odot}}, \\ &= (10.4 \pm 1.1) \times 10^{10}\,{\rm M}_{\odot}, \end{aligned} \quad \text{(B10)}$$

an increase of approximately 70% from the value still in stars today!

### B.3. *Normalisation summary*

Finally, we can substitute Equations B3 and B7 into B1 and write that the overall normalisation of the detection rate is calculated as

$$\begin{aligned} N_{\rm detect} &= f_{\rm detect} \cdot 10.4 \times 10^{10}\,{\rm M}_{\odot} \\ &\times \sum_{Z=Z_{\rm min}}^{Z_{\rm max}} p_Z \left( \sum_{i=1}^{N_{\rm binaries,Z}} w_i \theta_{\rm target,i} \right) \\ &\times \left( \frac{\langle m \rangle_{\rm COMPAS,Z}}{f_{\rm trunc}} \sum_{i=1}^{N_{\rm binaries,Z}} w_i \right)^{-1}. \end{aligned} \quad \text{(B11)}$$

## C. ASSESSING THE IMPACT OF MILKY WAY MODEL CHOICES

The model that we use for the Milky Way adds several layers of complexity, accounting for the inside-out growth of the thin disc, using empirically informed star formation histories that are a function of time and assigning metallicities based on the position and age of binaries. In this section, we repeat our main analysis but instead apply a simpler model for the Milky Way in order to assess the effect of these added features. For this purpose, we use model for the Milky Way used in Breivik et al. (2020) as this is representative of the models used in most previous works.

Their model can be summarised as follows: the Milky Way is assumed to comprise of three components, a thin disc, a thick disc and a bulge. The spatial distributions and relative masses for these components are given in McMillan (2011). Breivik et al. (2020) assume constant star formation over 10 Gyr for the thin disc, a 1 Gyr burst of star formation 11 Gyr ago for the thick disc and a 1 Gyr burst of star formation 10 Gyr ago for the bulge. A major difference is that only two metallicities are used and they are assigned to binaries independent of age or position. Binaries formed in the thin disc and bulge are assumed to have a metallicity of $Z = 0.02$ and those formed in the thick disc are assumed to have $Z = 0.003$.

We show the spatial metallicity distribution for this model in Fig. 9 in the same form as Fig. 1 for ease of comparison between our models. The two main differences we can see between Fig. 1 and 9 are that the Breivik et al. (2020) model is more centrally concentrated and only has two fixed metallicity populations.

When applying this simpler Milky Way model in combination with our fiducial binary physics assumptions (model A), we find that the expected number of detections for BHBHs, BHNSs and NSNSs for a 4-year LISA mission is 39, 39 and 14 respectively. Thus the BHBH and BHNS detection rates are only marginally increased from our main findings, but the NSNS detection has increased by nearly a factor of 2.

Moreover, the distribution of parameters within the population, particularly the mass distributions, are notably disparate. By using only two fixed metallicity populations, unphysical artifacts are introduced into distribution of DCO masses (Kummer at al. (in prep)). For example, in Fig. 10, we show the black hole mass distribution produced by the simulation using the simple Milky Way model. Despite the fact that these KDEs use the same bandwidth as Fig. 3, the distributions show many more sharp transitions, which is a result of pileups occurring at specific masses for specific metallicities.

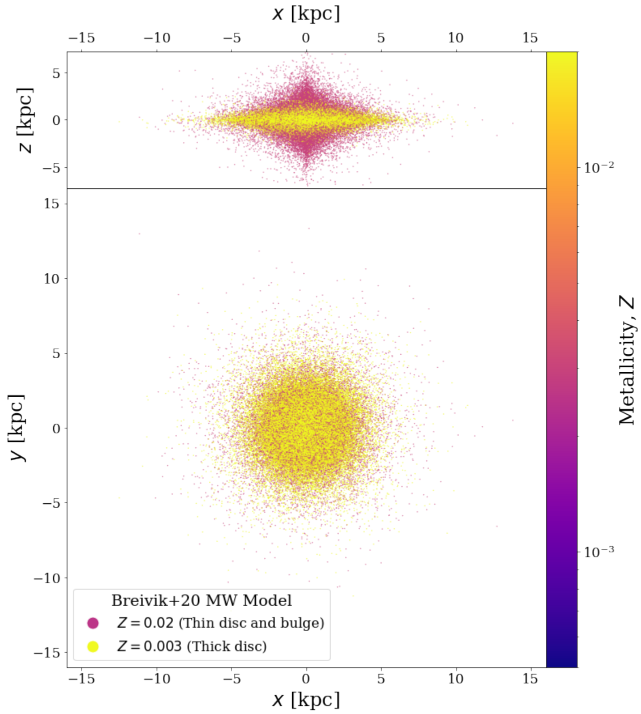


**Figure 9.** As Fig. 1 (right panel), but for the Milky Way model used in Breivik et al. (2020).

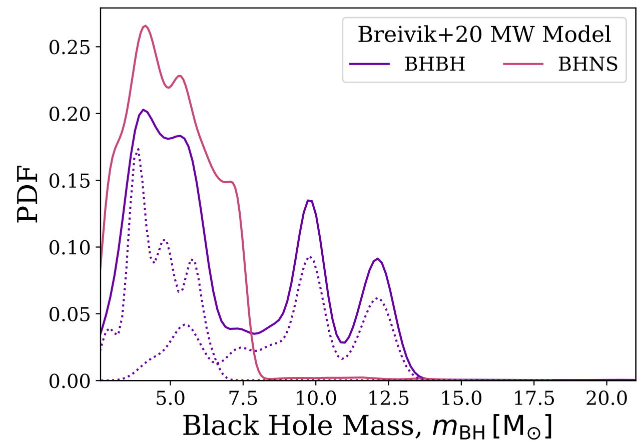


**Figure 10.** As Fig. 3 (top left panel), but for the Milky Way model used in Breivik et al. (2020).

Moreover, the lack of lower metallicities systems means that higher mass systems are not formed and so we see the distributions do not include a high mass tail such as in our fiducial results.

The unphysical artifacts present in the mass distributions can have far-reaching effects since the masses of DCOs affect most other parameters. The inspiral time and SNR are directly dependent on the mass, whilst the uncertainty estimates depend on the SNR. This means that the artifacts can affect the predictions for most distributions of LISA detectable populations.

Overall, we find that previous studies that use Milky Way models analogous to this simpler model may significantly overestimate the LISA NSNS detection rate as well as contain unphysical artifacts in their parameter distributions.

## D. ESTIMATING THE NUMBER OF PULSARS FOR A GIVEN SKY AREA IN SKA

In this section, we perform some back-of-the-envelope calculations in order to estimate the number of pulsars that SKA will observe within a given sky area.

First, we consider how many pulsars SKA is likely to detect. Keane et al. (2015) uses PSRPOPPy (Bates et al. 2014) to simulate the Milky Way pulsar population. They find that for SKA-1, approximately 10000 pulsars will be discovered. The second phase of SKA, which should be in operation by the time of the LISA mission, would yield a total of 35000-41000 pulsars (Keane et al. 2015). We use the average, 38000, in further estimates below. Moreover, we are only interested in pulsars that are part of a binary system. We estimate this pulsar binary fraction as the fraction of known pulsars that are in binaries using the ATNF Pulsar Catalogue[9] (Manchester et al. 2005). 290 of the 2872 currently known pulsars are in binary systems and thus we estimate the binary fraction of pulsars as 10%. Therefore, we expect that SKA-1 and SKA-2 will detect approximately 1000 and 3800 binary pulsars respectively.

Next, we can find the total number of pulsars SKA will detect in a patch on the sky. The total sky area that the SKA mission covers is approximately $5700\,\mathrm{deg}^2$, which is calculated by integrating over the sky for all Galactic longitudes and Galactic latitudes limited to $|b| < 10°$ and $\delta < 45°$, which are the limits on SKA-mid (Keane et al. 2015). If we assume that the pulsars are found uniformly across the sky, this means that roughly 0.2 and 0.7 binary pulsars are expected per square degree for SKA-1 and SKA-2 respectively. Note that the assumption of a uniform distribution is not realistic as pulsars will tend to be far more concentrated in the Galactic centre but we use it to provide an upper bound on these estimates.

Overall, we therefore expect a single pulsar per $5.7\,\mathrm{deg}^2$ and $1.5\,\mathrm{deg}^2$ for SKA-1 and SKA-2 respectively, which correspond to angular resolutions of $\sigma_\theta = 1.3°$ and $\sigma_\theta = 0.7°$.

[9] https://www.atnf.csiro.au/research/pulsar/psrcat

# E. SUPPLEMENTARY MATERIAL

## E.1. *Detection rate table*

**Table 2.** The number of detectable binaries in a 4- and 10-year LISA mission for the 20 different model variations and each DCO type. Each value shows the mean and the 90% confidence interval.

| Model | LISA (4 year) | | | LISA (10 year) | | |
|---|---|---|---|---|---|---|
| | BHBH | BHNS | NSNS | BHBH | BHNS | NSNS |
| A | $39.6^{+6.4}_{-6.6}$ | $36.5^{+6.5}_{-6.5}$ | $8.7^{+3.3}_{-2.7}$ | $62.9^{+8.1}_{-7.9}$ | $60.7^{+7.3}_{-7.7}$ | $14.4^{+3.6}_{-3.4}$ |
| B | $37.1^{+5.9}_{-6.1}$ | $17.4^{+4.6}_{-4.4}$ | $3.3^{+1.7}_{-2.3}$ | $58.7^{+7.3}_{-7.7}$ | $28.7^{+5.3}_{-5.7}$ | $5.3^{+2.7}_{-2.3}$ |
| C | $22.4^{+4.6}_{-4.4}$ | $5.8^{+2.2}_{-2.8}$ | $4.7^{+2.3}_{-1.7}$ | $35.8^{+6.2}_{-5.8}$ | $9.4^{+2.6}_{-3.4}$ | $7.6^{+2.4}_{-2.6}$ |
| D | $26.2^{+4.8}_{-5.2}$ | $4.3^{+1.7}_{-2.3}$ | $14.1^{+3.9}_{-4.1}$ | $40.5^{+6.5}_{-6.5}$ | $7.1^{+2.9}_{-3.1}$ | $23.2^{+4.8}_{-5.2}$ |
| E | $36.9^{+6.1}_{-5.9}$ | $4.2^{+1.8}_{-2.2}$ | $0.2^{+0.8}_{-0.2}$ | $58.6^{+7.4}_{-7.6}$ | $6.6^{+2.4}_{-2.6}$ | $0.3^{+0.7}_{-0.3}$ |
| F | $30.2^{+5.8}_{-5.2}$ | $22.9^{+5.1}_{-4.9}$ | $6.4^{+2.6}_{-2.4}$ | $47.5^{+6.5}_{-6.5}$ | $35.5^{+5.5}_{-5.5}$ | $10.4^{+3.6}_{-3.4}$ |
| G | $31.8^{+5.2}_{-5.8}$ | $25.9^{+5.1}_{-4.9}$ | $25.9^{+5.1}_{-4.9}$ | $50.5^{+7.5}_{-7.5}$ | $43.5^{+6.5}_{-6.5}$ | $42.4^{+6.6}_{-6.4}$ |
| H | $117.8^{+11.2}_{-10.8}$ | $51.7^{+7.3}_{-6.7}$ | $10.1^{+2.9}_{-3.1}$ | $181.6^{+13.4}_{-13.6}$ | $87.7^{+9.3}_{-9.7}$ | $16.7^{+4.3}_{-3.7}$ |
| I | $25.5^{+5.5}_{-5.5}$ | $62.0^{+8.0}_{-8.0}$ | $7.2^{+2.8}_{-2.2}$ | $39.1^{+5.9}_{-6.1}$ | $102.3^{+9.7}_{-10.3}$ | $11.9^{+3.1}_{-3.9}$ |
| J | $55.5^{+7.5}_{-7.5}$ | $27.9^{+5.1}_{-4.9}$ | $8.0^{+3.0}_{-3.0}$ | $87.8^{+9.2}_{-9.8}$ | $45.7^{+6.3}_{-6.7}$ | $13.0^{+4.0}_{-4.0}$ |
| K | $34.8^{+6.2}_{-5.8}$ | $42.4^{+6.6}_{-6.4}$ | $9.0^{+3.0}_{-3.0}$ | $56.0^{+7.0}_{-8.0}$ | $69.5^{+8.5}_{-8.5}$ | $14.8^{+4.2}_{-3.8}$ |
| L | $39.8^{+6.2}_{-6.8}$ | $36.7^{+6.3}_{-5.7}$ | $9.1^{+2.9}_{-3.1}$ | $63.4^{+7.6}_{-8.4}$ | $61.9^{+8.1}_{-7.9}$ | $14.7^{+3.3}_{-3.7}$ |
| M | $48.2^{+6.8}_{-7.2}$ | $80.8^{+9.2}_{-8.8}$ | $18.0^{+4.0}_{-4.0}$ | $75.3^{+8.7}_{-8.3}$ | $134.5^{+11.5}_{-11.5}$ | $29.5^{+5.5}_{-5.5}$ |
| N | $57.5^{+7.5}_{-7.5}$ | $138.2^{+11.8}_{-12.2}$ | $41.9^{+6.1}_{-6.9}$ | $89.5^{+9.5}_{-9.5}$ | $227.5^{+15.5}_{-15.5}$ | $67.4^{+8.6}_{-8.4}$ |
| O | $45.7^{+6.3}_{-6.7}$ | $85.3^{+9.7}_{-9.3}$ | $10.2^{+2.8}_{-3.2}$ | $70.9^{+8.1}_{-8.9}$ | $141.6^{+12.4}_{-11.6}$ | $16.8^{+4.2}_{-3.8}$ |
| P | $50.8^{+7.2}_{-6.8}$ | $32.7^{+5.3}_{-5.7}$ | $10.0^{+3.0}_{-3.0}$ | $77.6^{+8.4}_{-8.6}$ | $53.1^{+6.9}_{-7.1}$ | $16.5^{+4.5}_{-4.5}$ |
| Q | $0.0^{+0.0}_{-0.0}$ | $6.7^{+2.3}_{-2.7}$ | $8.5^{+2.5}_{-2.5}$ | $0.0^{+0.0}_{-0.0}$ | $11.3^{+3.7}_{-3.3}$ | $13.8^{+4.2}_{-3.8}$ |

## E.2. *Distribution of eccentric sources on sensitivity curve*

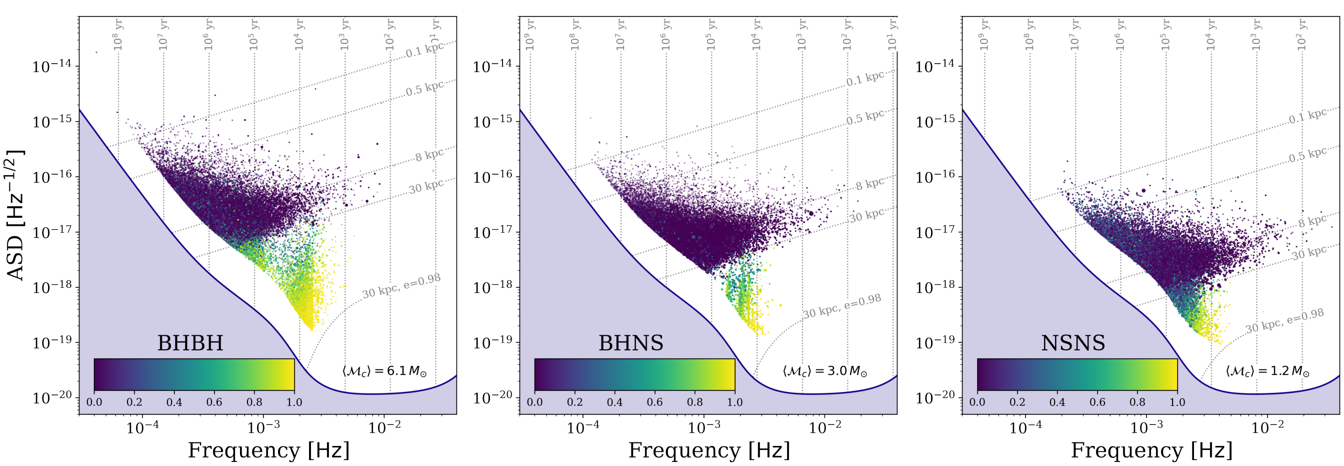


**Figure 11.** As the bottom panels of Fig. 2, but without the density distributions and scatter points are coloured by their eccentricity. We show eccentric sources are located in an offshoot below the 30 kpc around 2 mHz.

### E.3. *Formation channels*

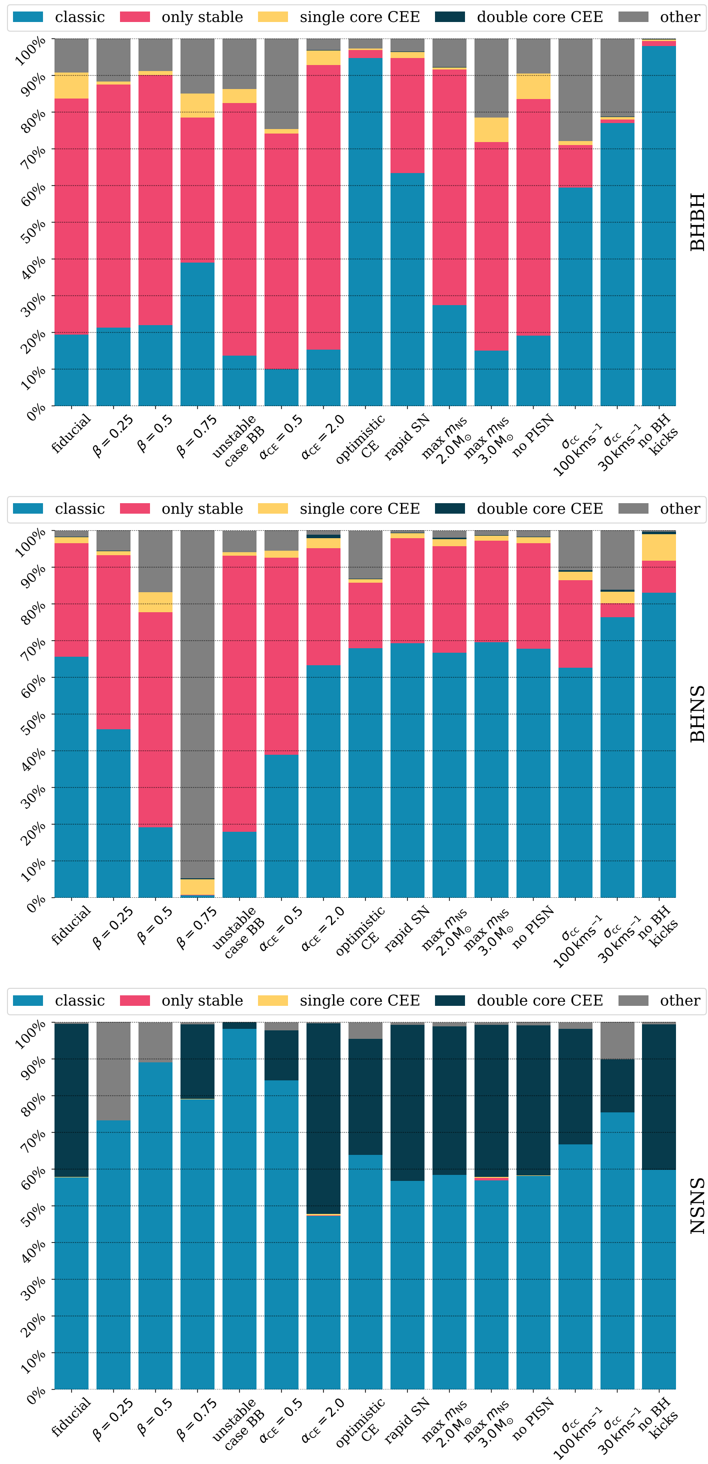


**Figure 12.** Fraction of each DCO type that is formed through different formation channels for all physics variations. Channels are described in detail in Broekgaarden et al. (2021). The classic, single core CEE and double core CEE channels all require at least one common envelope event whilst only 'only stable' consists of only stable mass transfer and 'other' contains the remaining binaries which are mainly formed from 'lucky' supernova kicks that shrink the binary. [TODO: Update with new models]